Journal of Nanobiotechnology

REVIEW

Open Access

Shedding light on vascular imaging: the revolutionary role of nanotechnology

Peisen Zhang[1,2], Yao Li[1], Xiaoqi Li[1], Yudong Wang[1], Hua Lin[3], Ni Zhang[3], Wenyue Li[2], Lihong Jing[4], Mingxia Jiao[1*], Xiliang Luo[1*] and Yi Hou[2*]

Abstract

Vascular dysfunction, characterized by changes in anatomy, hemodynamics, and molecular expressions of vasculatures, is closely linked to the onset and development of diseases, emphasizing the importance of its detection. In clinical practice, medical imaging has been utilized as a significant tool in the assessment of vascular dysfunction, however, traditional imaging techniques still lack sufficient resolution for visualizing the complex microvascular systems. Over the past decade, with the rapid advancement of nanotechnology and the emergence of corresponding detection facilities, engineered nanomaterials offer new alternatives to traditional contrast agents. Compared with conventional small molecule counterparts, nanomaterials possess numerous advantages for vascular imaging, holding the potential to significantly advance related technologies. In this review, the latest developments in nanotechnology-assisted vascular imaging research across different imaging modalities, including contrast-enhanced magnetic resonance (MR) angiography, susceptibility-weighted imaging (SWI), and fluorescence imaging in the second near-infrared window (NIR-II) are summarized. Additionally, the advancements of preclinical and clinical studies related to these nanotechnology-enhanced vascular imaging approaches are outlined, with subsequent discussion on the current challenges and future prospects in both basic research and clinical translation.

Keywords Vascular dysfunction, Nanomaterials, MR angiography, Susceptibility-weighted imaging, Fluorescence imaging

*Correspondence:
Mingxia Jiao
jiaomingxia@qust.edu.cn
Xiliang Luo
xiliangluo@qust.edu.cn
Yi Hou
houyi@iccas.ac.cn
Full list of author information is available at the end of the article

Graphical Abstract

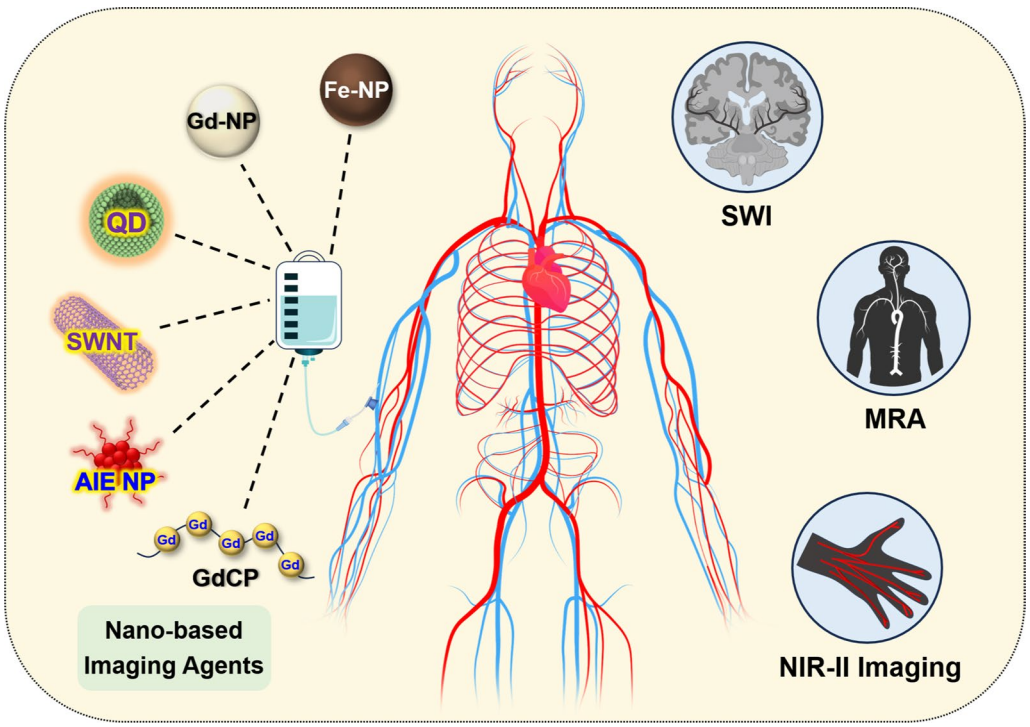

Background

Vascular dysfunctions, which involve pathological changes in vascular anatomy, shifts in hemodynamics, and abnormal molecular expressions, are intricately associated with the onset and progression of diverse diseases [1]. For example, the atherosclerotic plaque may lead to the stenosis of the vascular lumen [2–4]; the myocardial infarction and ischemic cerebral infarction originate from vascular occlusion [5, 6]; the development of malignant tumors is usually accompanied by angiogenesis and vascular malformation [7, 8]; and the inflammation may induce the over-expression of various enzymes and biological factors, subsequently leading to the enhancement of vascular permeability [9]. Within this context, the precise detection of vascular abnormalities plays an important role in guiding the clinical management and intervention of the related diseases.

Medical imaging is one of the mainstays of the diagnosis of vascular dysfunctions. In clinical practice, different imaging modalities, such as ultrasound imaging, digital subtraction angiography (DSA), magnetic resonance imaging (MRI), or computed tomography (CT), have been employed to intuitively visualize the anatomical change of vasculatures [10, 11]. For examples, ultrasound imaging can detect the vascular structures and blood flow status by using sound waves, and generate real-time images on the basis of different echo characteristics of vessels and other tissues [12, 13]. MR angiography employs magnetic fields and radio frequency pulse to map out the detailed images of blood vessels in vivo without ionizing radiation [14], while CT angiography uses X-rays to generate cross-sectional images, allowing for the assessment of the vascular conditions [15]. In addition to the clinically compatible imaging modalities that have been widely utilized in clinical settings, fluorescence-based optical imaging modality has also attracted significant attention for disease diagnosis over the past two decades due to its high sensitivity and real-time feedback capability [16]. Particularly, fluorescence imaging in the near-infrared II region (1000–1700 nm) has been demonstrated to exhibit improved tissue penetration depth and reduction of tissue autofluorescence, which enables the high-resolution imaging of superficial vasculatures in vivo [1, 17]. The NIR-II fluorescence imaging is currently undergoing laboratory and preclinical studies, and is likely to become one of the medical imaging techniques for clinical vascular imaging in the future.

To obtain a more detailed visualization of physiological/pathological structures of different tissues, contrast agents are employed to enhance the contrast in the images in diverse medical imaging modalities [18, 19]. This heightened imaging quality facilitates the clinicians to make a more refined and accurate evaluation of the patient's medical status. For vascular imaging, the utilization of appropriate contrast agents can significantly increase the resolution of tiny vessels, enabling a more accurate diagnosis of vascular abnormalities.

Over the past several decades, with the rapid advancement of nanotechnology, coupled with corresponding detection methods and supporting facilities, engineered nanomaterials have offered new alternatives for conventional contrast agents [3, 20–23]. In comparison to the small-molecular formulations, nanomaterials typically possess longer blood circulation time without vascular leakage, because their nano-scale hydrodynamic diameters are larger than the intercellular junctions between capillary endothelial cells (approximately 6 nm in postcapillary venules) [24]. This characteristic provides an extended timeframe for vascular imaging, enabling high-resolution visualization of vascular anatomical structures and facilitating real-time monitoring of hemodynamic changes over a prolonged duration. Meanwhile, the non-extravasating nature of nanomaterials, and the consequent high contrast-to-noise ratio, further enhance the resolution and accuracy of vascular imaging. Additionally, distinctive physicochemical characteristics arising from the size effects of nanomaterials enable a more extensive and intricate integration of biomedical functionalities, thereby allowing for a more comprehensive detection of both vascular anatomical and pathological abnormalities [25, 26]. Due to these benefits, nanomaterials have been exploited as imaging agents for vascular imaging across various imaging modalities. The performance of these nanoagents has undergone comprehensive investigation by researchers in the fields of chemistry, materials science, and medicine.

In this review, the latest advancements in laboratory research on vascular imaging in different modalities based on nanotechnology were summarized, with a particular emphasis on the outstanding application of nanomaterials in this field. Simultaneously, this review also provides an overview of the corresponding progress in preclinical and clinical studies related to these nanotechnology-based vascular imaging methods (Fig. 1). Additionally, the current challenges and future

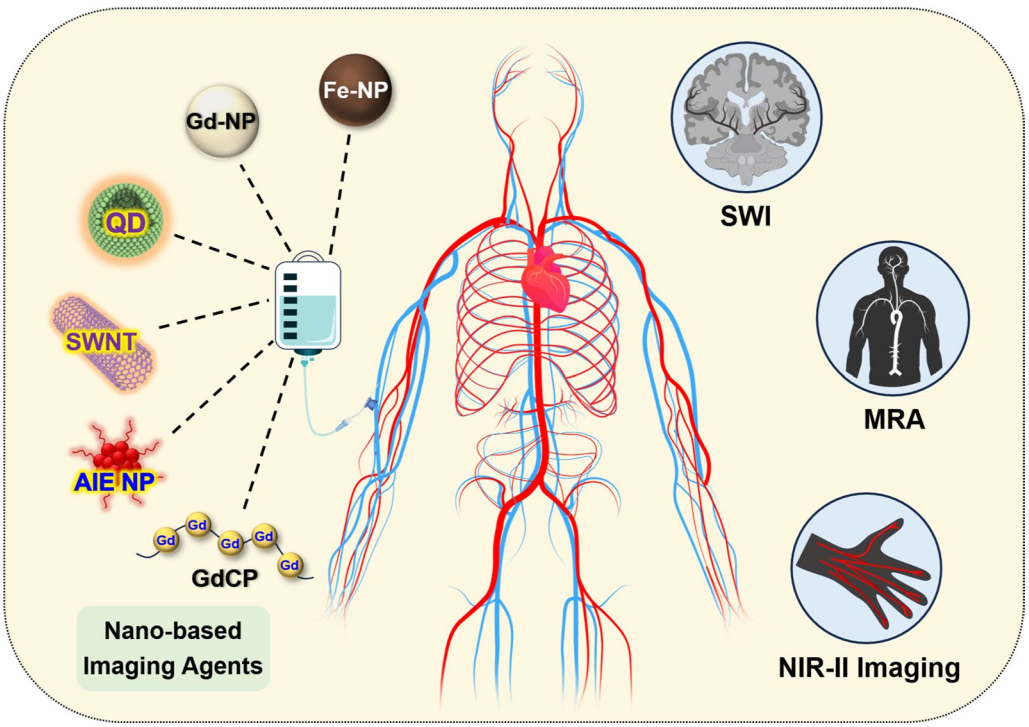

Fig. 1 The versatile vascular imaging strategies based on various nanomaterials. *Fe-NP* Fe-based nanoparticle, *Gd-NP* Gd-based nanoparticle, *QD* quantum dot, *SWNT* single-walled carbon nanotube, *AIE NP* aggregation-induced emission nanoparticle, *GdCP* Gd^{3+} chelating polymer, *SWI* susceptibility-weighted imaging, *MRA* magnetic resonance angiography, *NIR-II Imaging* imaging in the second near-infrared window

perspectives are also discussed for both fundamental studies and clinical translation.

Vascular imaging with MRI

MRI, founded on the principles of nuclear magnetic resonance (NMR), stands as a potent imaging technology extensively applied for the noninvasive disease diagnosis in clinical settings. Over the past several decades, this imaging modality has emerged as the optimal choice for imaging deep-seated vasculature within the body owing to its unrestricted tissue penetration, exceptional spatial resolution, and superior soft tissue contrast [27]. Especially in recent years, MRI techniques integrated with nanomaterials have surfaced as exceptionally promising platforms to elevate the quality of vascular imaging, particularly with regards to improving both resolution and sensitivity [28–30].

3D vascular imaging with contrast-enhanced (CE) MR angiography (MRA)

MR angiography (MRA) is a noninvasive imaging technology for vascular visualization based on MRI, which relies on the properties of hydrogen atoms in the bloodstream to generate detailed angiograms. Over the last two decades, non-contrast MRA has emerged as a valuable tool in clinical practice for evaluating arterial diseases [31, 32]. By leveraging its ability to differentiate flowing spins in blood from those in stationary tissue, non-contrast MRA allows for the visualization of hemodynamic flow [33]. For examples, time-of-flight (TOF) MRA and phase contrast (PC) MRA have been demonstrated to provide essential perspectives of the vascular malformation, hemodynamic flow variations, and recanalization status, largely improving patient care and outcomes. Nevertheless, these non-contrast enhanced MRA sequences still face the challenges owing to the inherent principles of imaging. The blood flow dependency of the vascular signals makes it hard in achieving satisfactory delineation of the micro-vessels with complicated structures or the venous vessels with low blood flow velocity. Specifically, the vessels parallel to the scanning plane is difficult to be depicted, since the blood flow velocity perpendicular to the scanning plane is rather low [34, 35].

In this context, the contrast-enhanced (CE) MRA has been exploited for better visualizing the micro-vasculatures with the appropriate T_1 contrast agents. Compared to the non-contrast-enhanced MRA, CE MRA generates the vascular contrast through the shortening of the T_1 relaxation time of the blood in vessels, relatively less dependent to the blood flow velocity [36, 37]. Therefore, CE MRA can exhibit an improved anatomical coverage of the vascular systems, in which the micro-vessels with complicated structures or veins with low blood flow velocity can be better visualized.

The quality of the contrast agent is one of the decisive factors in determining the effectiveness of CE MRA images. In clinical practice, a series of polyamino polycarboxylic chelates of gadolinium ions (Gd^{3+}) have been developed as the predominant paramagnetic contrast agents [38]. These agents have been proven highly effective in achieving desirable T_1 contrast effects in MRI [39, 40]. Nevertheless, there are certain drawbacks associated with small molecular Gd-chelate contrast agents that impede their clinical applications in MRA. Due to their small hydrodynamic sizes, these currently available clinical small-molecular-weight contrast agents possess short tumbling times (τ_R), resulting in relatively low longitudinal molar relaxivities (r_1) [41]. Additionally, the small molecular Gd-chelates have a tendency to extravasate from blood vessels quickly and eliminate through the renal system within several minutes, leading to a very short blood circulation time [42, 43]. Consequently, high-resolution MRA, especially for the visualization of tiny blood vessels, remains a significant challenge. In contrast, nanomaterials offer several advantages that address these issues effectively. First, the larger size of nanoparticles results in slower renal clearance and prolonged circulation times, enhancing vascular retention time and providing extended imaging windows for better resolution of small and deep blood vessels. Additionally, nanoparticles exhibit higher longitudinal molar relaxivity (r_1), leading to stronger, more stable T_1 contrast. Furthermore, nanomaterials can be functionalized with targeting moieties, enabling specific binding to endothelial cells or other vascular structures, which improves the accuracy and sensitivity of MRA. These advantages make nanomaterials highly promising alternatives to small-molecule contrast agents in advanced MRA applications.

Gd^{3+} chelating polymer (GdCP) nanomaterials

Polymers are ideal candidates as materials for constructing nano-contrast agents. Specifically, individual Gd^{3+} ions can be integrated into one nanoscale polymer framework, resulting in a nanosized contrast agent, known as Gd^{3+} chelating polymer (GdCP) nanomaterials. Compared to their small-molecule Gd^{3+} counterparts, GdCP contrast agents offer advantages such as prolonged longitudinal τ_R and extended blood circulation times, which contribute to enhanced resolution in angiographic imaging. Based on this strategy, Luo et al. synthesized a polymeric micelle contrast agent derived from the self-assembly of block and amphiphilic polymer pGFLG-block-pHPMA-DOTA-Gd. This contrast agent demonstrated elevated longitudinal relaxivity of 10.9 mM^{-1} s^{-1}

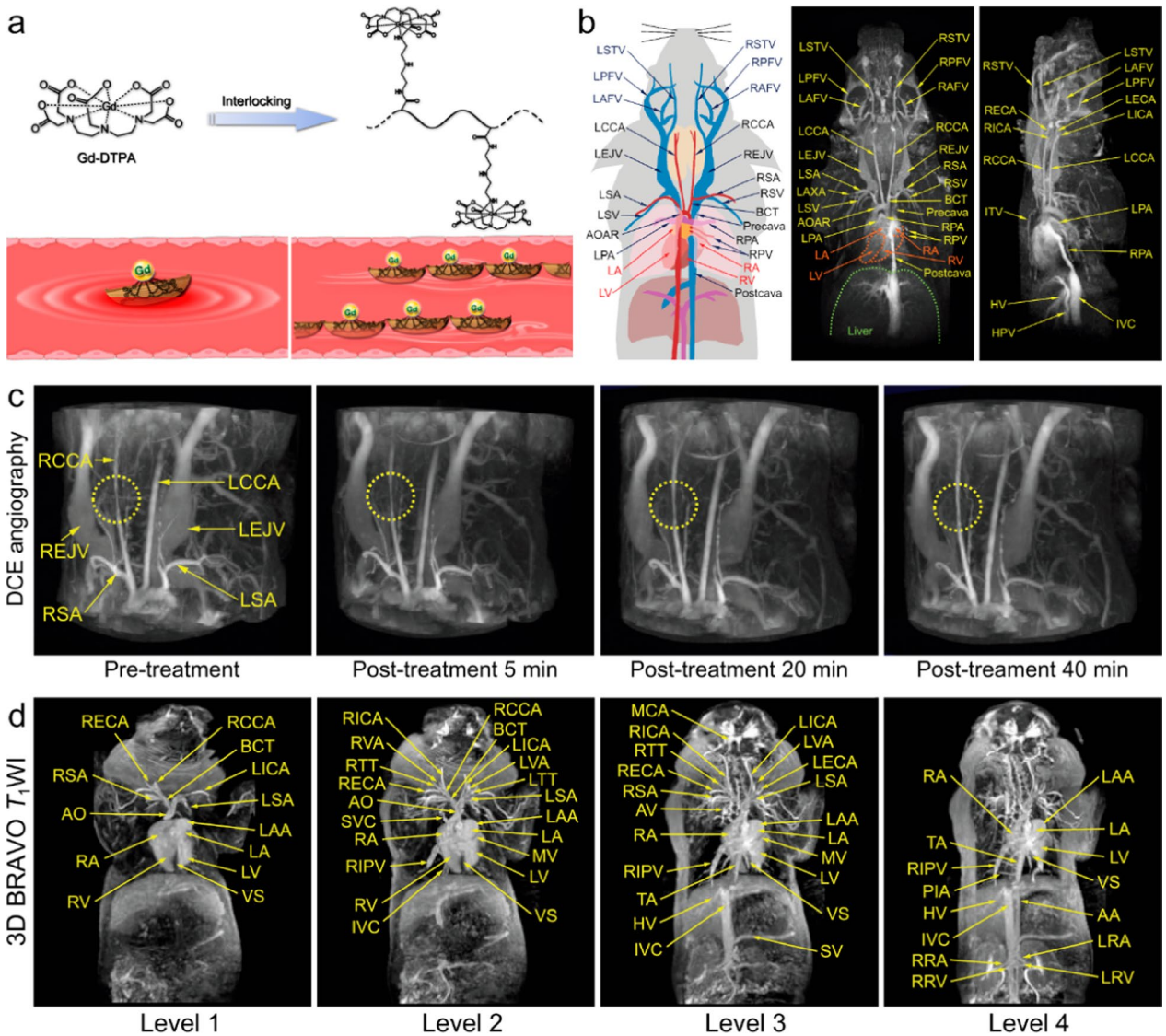

Fig. 2 **a** The schematic illustration of zwitterionic polymeric MR contrast agents PAA-Gd compared with individual Gd-DTPA. **b** Schematic drawing of vascular anatomy and the vascular identification in different directions of 3D angiography of mouse body. **c** PAA-Gd enhanced 3D angiography of mouse carotid thrombosis pre-treatment (obtained at 5 min after PAA-Gd injection), and the real-time monitoring of thrombolytic therapy post-treatment of urokinase-type plasminogen activator (uPA). (The carotid thrombosis was identified by yellow dotted circle). **d** Different coronal levels of 3D BRAVO images of swine for identifying the vascular structures. Reproduced with permission from Hou et al. [45]

and prolonged blood half-life of 161 min in mice, significantly surpassing the performance of clinically used Gd-DTPA (3.4 mM^{-1} s^{-1}, 14 min). Using this polymeric contrast agent, the anatomical structures of abdominal, intracranial and tumoral vasculatures can be readily delineated [44]. Near recently, Hou et al. proposed a hypersensitive MRA strategy inspired by the Chinese historical story of interlocking stratagem. Specifically, they designed and synthesized a nanoscale macromolecule with a zwitterionic structure to serve as a polymeric MRA contrast agent. In this approach, Gd-DTPA molecules were assembled through covalent bonding to the side chains of poly(acrylic acid) (PAA) molecules using diethylenetriamine (DET) crosslinkers. The combination of the negatively charged carboxyl group at the DTPA terminal and the positively charged secondary amine group in the DET linker results in the zwitterionic structure of the contrast agent (Fig. 2a). Owing to the integration of Gd^{3+} within a single polymeric molecule, the r_1 of PAA-Gd achieved a notable value of 13.9 mM^{-1} s^{-1} when examined under a 1.5 T clinical MRI scanner. Additionally, the hydrodynamic diameter of PAA-Gd was determined to

be 7.7 nm. With the nanosized diameter and zwitterionic structure, PAA-Gd can avoid being captured by immune system and maintained within the vascular lumen without extravasation, offering a sufficient angiography window. Additionally, PAA-Gd has been demonstrated to be fluidly cleared by the kidneys without undesired body retentions. In the rodent models, the sophisticated three-dimensional microvascular structures in the head, thorax, and abdomen of rodents can be delineated, achieving a maximum resolution of less than 100 μm (Fig. 2b). This imaging capability extends to the precise identification of atherosclerotic plaques and the real-time monitoring of the entire thrombolytic treatment process using just a single injection (Fig. 2c). For further verifying the clinical translation prospects of PAA-Gd, the angiography performances and biosafety features on large mammals were systematically investigated. The results revealed that the PAA-Gd exhibited outstanding vascular imaging performance on swine under a 3.0 T human MRI scanner (Fig. 2d), and the administration of PAA-Gd did not induce any abnormalities in the swine's physiological parameters [45]. Very recently, Hou's group further extended the PAA-Gd-based angiography strategy to the field of oncology. Unlike the relatively well-organized cardiovascular structures, imaging tumor blood vessels presents a more complex challenge due to the chaotic, abnormal, and disorganized nature of these vessels, along with unpredictable blood flow velocities. Leveraging the superior angiographic performance of PAA-Gd, the high-resolution 3D visualization of the spatiotemporal distribution of intricate microvasculature in solid tumors—formed by various cell lines over different inoculation times—were successfully achieved [46].

Inorganic Gd-based nanoparticles

In addition to the Gd-chelating polymer contrast agent, Gd-based inorganic nanoparticles has been also used as contrast agents in the MRA. With the substantial surface Gd^{3+} and nano-sized hydrodynamic diameter, the Gd-based inorganic nanoparticles demonstrated elevated longitudinal relaxivity and protracted blood circulation time. These characteristics aligns with the requirements of high-resolution angiography, further enhancing the effectiveness and precision of the imaging process. Among the different Gd-based nanoparticles, inorganic fluorides such as $NaGdF_4$ nanomaterials can be readily prepared by pyrolysis methods with tunable diameters and narrow size distributions. In 2014, Shi et al. prepared ultrasmall $NaGdF_4$ nanodots with the diameter of ~2 nm with PEG coating. To avoid the toxicity associated with the potentially released free Gd^{3+} ions, DTPA molecules were modified onto the surface of nanodots as Gd^{3+} capture agents. The resultant nanoparticles can be served as contrast agents to achieve efficient MRA and atherosclerotic plaque diagnosis [47]. In the subsequent work, Yao et al. prepared PEGylated biocompatible $NaYF_4$:Yb/Er@$NaGdF_4$ nanoparticles and successfully realize the vasculature imaging on rats, improving the diagnostic efficiency of acute ischemic stroke [48]. Very recently, Han et al. synthesized ultrasmall $NaGdF_4$ nanoparticles with the diameter of ~3.5 nm, and coated the red blood cell membrane to endow the nanoparticles with stealth nature to evade the host immune system. The resultant nano-sized contrast agent $NaGdF_4$@RBCm showcased long blood half-life of 357.5 min, allowing for the long-time-window visualization of the 3D vascular structures of rodent animals. With this imaging property, the blockage and recanalization of carotid artery in mice can be serially monitored following a single intravenous administration [49].

In addition to the fluorides, other types of Gd-doped nanomaterials have also been explored as contrast agent of angiography. Lu et al. prepared Gd^{3+}-doped CaF_2-based core–shell nanoparticles (CaF_2:Yb,Er@CaF_2:Gd), which exhibited high longitudinal relaxivity of 21.86 mM^{-1} s^{-1} under 3.0 T MRI scanner, successfully realizing the whole body angiography of mice [50]. In another study, Lin et al. prepared citrate-coated Gd-doped TiO_2 ellipsoidal nanoparticles (GdTi-SC NPs). Under the irradiation of UV, local superhydrophilic regions were generated on the surface of GdTi-SC NPs, significantly enhancing the r_1 of the nanoparticles. Upon the intravenous administration, this Gd-doped nano-sized contrast agent showcased well MRA performance for depicting the anatomical structures of vessels and detecting the vascular occlusion in rats [51]. Yu et al. synthesized the Gd-doped paramagnetic amorphous carbonate nanoclusters (ACNC) based on the mutual effect between Gd^{3+} and the formation of amorphous $CaCO_3$. Benefiting from the advantages of facile the one-pot synthesis, this nanomaterial can be readily prepared in large scale and served as MRI contrast agent for angiography (Fig. 3a). Upon the intravenous administration, the vasculature structures in various mammals including rat, rabbit, and dog, can be successfully depicted, showcasing its superior imaging performance compared to Gd-DTPA (Fig. 3b) [52]. Very recently, Zhang et al. developed albumin-coated gadolinium-based nanoparticles (BSA-Gd) as a contrast agent for achieving ultra-high-resolution MRA. This Gd-based nano-contrast agent demonstrated enhanced MRI performance, enabling high-resolution imaging of blood vessels in different animals including rats, rabbits, and beagles. It successfully visualized vessels of sub-200 μm in both normal tissue and tumors using

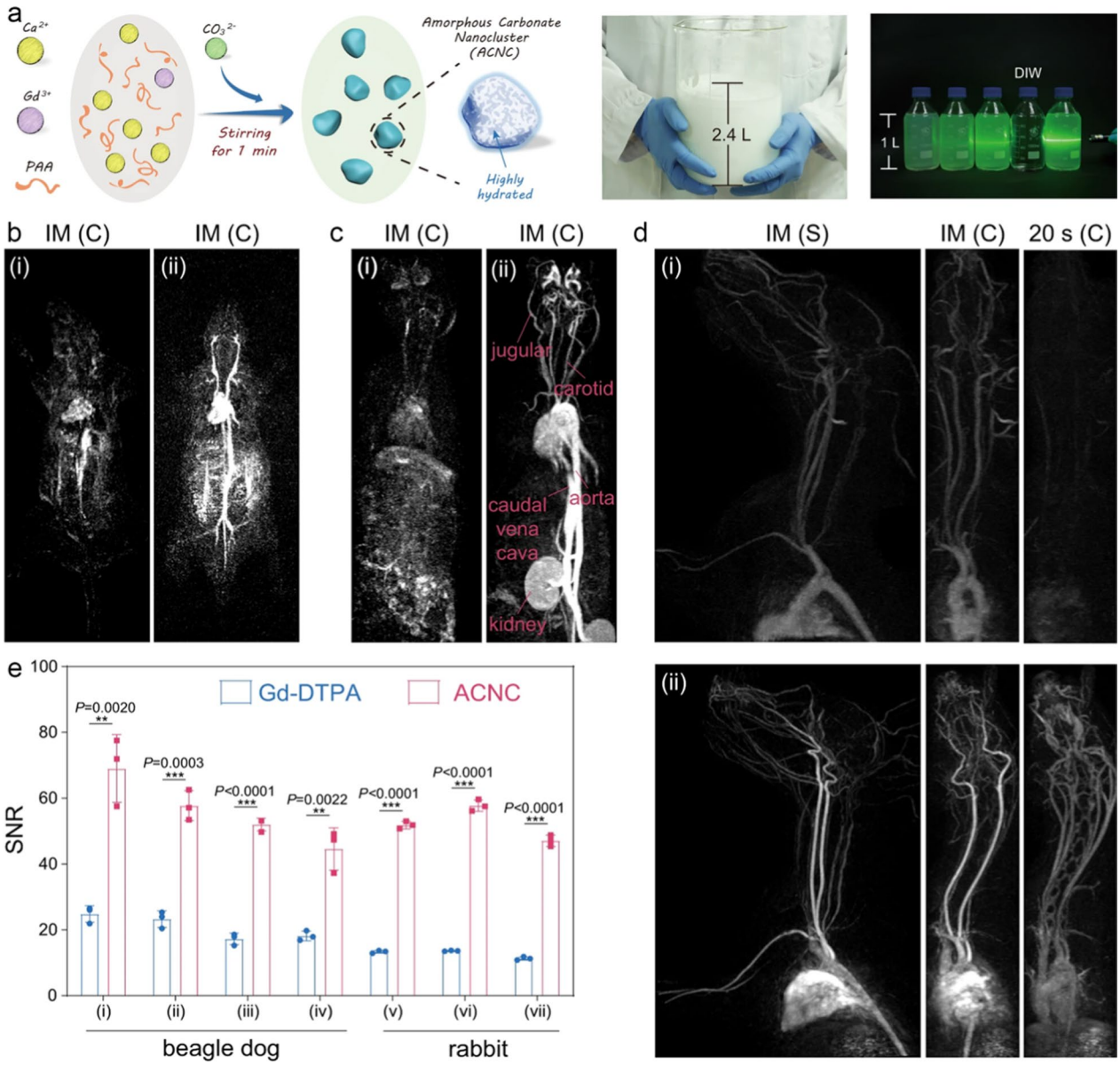

Fig. 3 **a** Scheme of the synthesis process of ACNC and the large-scale prepared ACNC. Contrast-enhanced MRA images of the whole body on **b** rat and **c** rabbit immediately after the bolus injection of (i) Gd-DTPA and (ii) ACNC. **d** MRA images of upper body on beagle dog at immediately (IM) and 20 s after the bolus injection of (i) Gd-DTPA and (ii) ACNC, respectively. (C) and (S) represents coronal plane and sagittal plane respectively. **e** Quantitative measurement of SNR of ROIs in (i) brachiocephalic trunk artery, (ii) left subclavian artery, (iii) left common carotid artery, (iv) right branch of olfactory artery of beagle dog, and that in (v) descending aorta, (vi) aortic arch, (vii) ascending aorta of rabbit, respectively. Reproduced with permission from Yu et al. [52]

3 T MRI, offering a valuable tool for advancing the study of vascular diseases [53].

Inorganic Fe-based nanoparticles

Apart from Gd-based nanoparticles, Fe-based nanoparticles have also shown promising performance in MRA owing to the 5 unpaired electrons of Fe^{3+} ion. Cheon et al. reported a nanosized Fe-based contrast agent consist of a polysaccharide supramolecular core and an amorphous-like hydrous ferric oxide shell, known as SAIO, which exhibited strong T_1 MRI effect. In the SAIO-enhanced angiography, the cerebral, coronary, and peripheral microvessels with the order of 100 μm in the rodents are discernible with remarkable clarity. Additionally, following the intravenously injection, the SAIO can be readily eliminated by the urinary system without

undesired organ retention, which highlights the biosafety profile of this contrast agent [54].

Among different Fe-based nanosized contrast agents, superparamagnetic iron oxide nanoparticles, exemplified by Feridex or Resovist, had been served as prominent T_2 contrast agents in clinical MRI diagnosis owing to their strong magnetic moments [55–57]. Interestingly, as their sizes diminish, the magnetic moment of iron oxide nanoparticles will rapidly decrease as a result of the reduction in the volume magnetic anisotropy and spin disorders on the nanoparticle surface. With regards to this phenomenon, the small-sized iron oxide nanoparticles can emerge as promising candidates for T_1 contrast agents, potentially utilized in MRA [58, 59]. Based on this principle, Hyeon et al. synthesized the extremely small-sized iron oxide nanoparticles (ESION) with the diameter of less than 4 nm. Owing to their tiny sizes, these nanoparticles exhibited very low magnetization but high T_1 MRI contrast effect. With high r_1 and long blood half-life, ESION facilitated the blood pool MRI of the anatomical structures of vasculatures, and the microvessels with the diameter of 0.2 mm could be delineated with precision [60]. In the subsequent studies, they further realized the large-scaled synthesis of the PEGylated iron oxide nanoclusters (PEG-IONCs), and successfully utilized these nanoparticles for MRA of large mammals including beagle dos and macaques. Moreover, the biosafety profiles of these nanoparticles have been effectively confirmed in dog and macaque models [61].

According to both preclinical and clinical reports, iron oxide nanoparticles appear to demonstrate superior biocompatibility and biosafety compared to Gd-based materials. This distinction arises from the potential adverse side effects associated with Gd^{3+} deposition, whereas iron species are naturally abundant in the human body. Until now, there have been clinical investigations employing iron oxide nanoparticles for the purpose of vascular imaging. As a typical example, Ferumoxytol (Feraheme, AMAG Pharmaceuticals, Waltham, MA) is an ultrasmall superparamagnetic iron oxide agent initially approved by the Food and Drug Administration (FDA) as an iron replacement therapy for patients with anemia due to chronic renal failure [62, 63]. Over the past decade, Ferumoxytol has been investigated extensively as an intravenous contrast agent in MRA [64, 65]. Owing to the nano-sized diameter and carbohydrate coating, Ferumoxytol exhibited an ultra-long blood circulation time exceeding 14 h in human, which provide an ample time period for acquiring high-resolution angiograms in both arterial and venous imaging with suitable MRI sequences [66, 67]. In previous publications, various research groups and clinicians have explored the application of Ferumoxytol in human vascular MRI. For example, the aorta and its major branches in a 90-year-old adult was successfully visualized following the intravenous administration of Ferumoxytol (Fig. 4a–e). In another case, the cardiac angiography of a 19-month-old male patient can also be displayed to make more comprehensive evaluation of the anatomical structures of cardiac vessels though ferumoxytol-enhanced 4D MRA with Multiphase Steady-state Imaging with Contrast (MUSIC) technique (Fig. 4f and g) [68]. Overall, Ferumoxytol has demonstrated satisfactory MRA performances in human, drawing immediate attention for its angiography application [68, 69]. Although the FDA issued a warning regarding the risk of acute hypersensitivity reactions during rapid high-dose injections, some subsequent studies involving large patient cohorts have shown that diagnostic use of Ferumoxytol was well-tolerated, with minimal adverse reactions, and severe events are rare [70–72]. Building upon these studies and clinical practice outcomes, Ferumoxytol presents an appealing alternative to Gd-based agents in MR angiography, particularly for children and patients with chronic kidney disease, because the Ferumoxytol can bypass the kidney filtration and do not contain toxic Gd.

Cerebrovascular imaging with nanomaterials-enhanced susceptibility-weighted imaging (SWI)

Apart from the CE MRA, susceptibility-weighted imaging (SWI) has emerged as a crucial component of the MRI approach for evaluating the vascular diseases, especially the cerebrovascular diseases [73–75]. SWI belongs to the category of gradient recalled echo T_2^*-weighted imaging and is highly sensitive to the deoxyhemoglobin within the cerebral bloodstream [76, 77]. In particular, this sequence exhibits remarkable sensitivity to the variation of deoxyhemoglobin levels, which offers valuable insights into tissue injury and cerebral oxygenation. Notably, regions affected by injury often exhibit an elevated oxygen extraction fraction, resulting in a significant increase in deoxyhemoglobin concentration. Consequently, the T_2^* relaxation of blood vessels within these regions usually shortened, leading to robust negative vascular signals in SWI. This phenomenon, commonly referred to as the blood oxygen level dependent (BOLD) effect, enables the visualization and characterization of cerebral small veins with high accuracy and sensitivity [78–80]. SWI's ability to capture the BOLD effect makes it an indispensable tool for assessing patients with cerebrovascular diseases in clinical practice.

Nevertheless, non-contrast SWI struggles to distinguish microvessels in the range of 50–100 μm, which may be the pathological scale for many microvascular diseases [81]. Additionally, the inherent vascular contrast

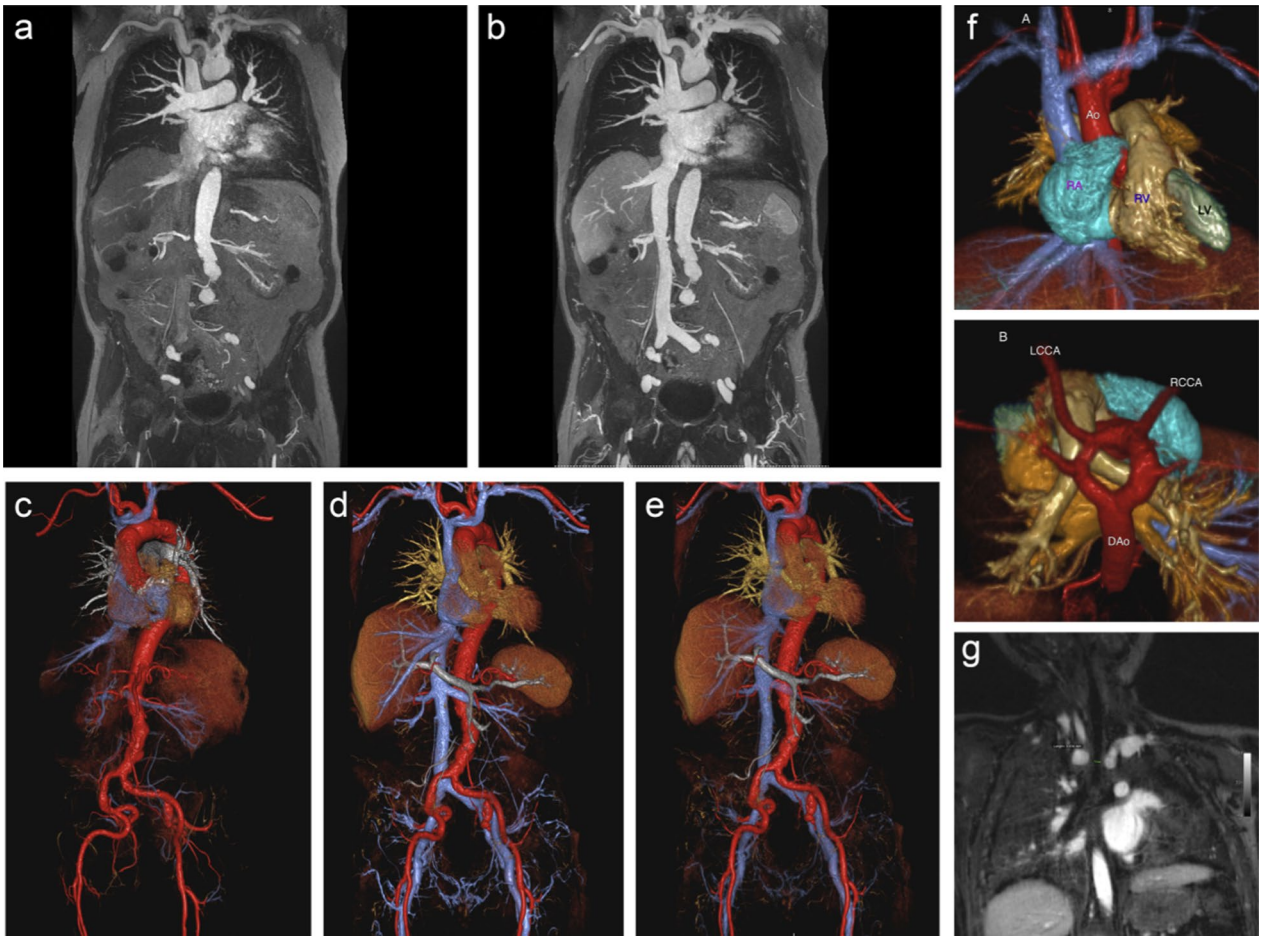

Fig. 4 **a**–**e** A 90-year-old man with renal failure undergoing vascular evaluation for transcatheter aortic valve replacement (TAVR). First-pass imaging with ferumoxytol on thin maximum intensity projection (MIP) **a** and volume rendered (VR) **c** reconstructions shows similar bright and uniform arterial enhancement as on steady-state images **b**, **d**, **e**, where arteries and veins show equal signal intensity. **f**, **g** A 19-month-old male patient with stridor and no prior history of congenital heart disease. Volume-rendered reconstruction from a single frame of a 4D MUSIC acquisition **f** from the anterior (upper) and superior (lower) perspective show a complete vascular ring due to a double arch, with normal cardiac chamber anatomy. Dynamic evaluation of the 4D MUSIC data confirmed compression of the trachea **g**. These images were acquired at 3T. Reproduced with permission from Finn et al. [68]

provided by endogenous deoxyhemoglobin remains insufficient to achieve high-resolution depiction of intricate small cerebral vessels, especially for arteries. In order to overcome this constraint, nanoparticle-based contrast agents were explored to enhance the sensitivity of SWI in detecting micro-vessels. In particular, owing to the exceptional superparamagnetic properties, Fe_3O_4 nanoparticles-based contrast agents have demonstrated remarkable potential for improving SWI performance. When compared to endogenous deoxyhemoglobin, the superparamagnetic Fe_3O_4 nanoparticles exhibit a much more pronounced effect on shortening the T_2^* relaxation time of the bloodstream, thereby producing significantly negative vascular signals in SWI [82, 83]. By employing Fe_3O_4 nanoparticles as contrast agents, the sensitivity of SWI can be greatly enhanced, enabling a more detailed and accurate depiction of microvascular structures. The unique superparamagnetism exhibited by these nanoparticles makes them an excellent choice for augmenting the capabilities of SWI and advancing its clinical utility.

In recent years, Fe_3O_4 nanoparticles-based SWI strategy has been explored to enhance the delineation of cerebral vessels, thereby achieving a more comprehensive diagnosis of brain diseases by providing improved imaging clarity. For example, after the onset of acute ischemic stroke, the vessels surrounding the blocked arteries undergo dilation and anastomosis, forming collateral vessels. These collateral vessels serve to compensate for the reduced blood supply to the ischemic brain tissues. Gao et al. synthesized $\alpha_v\beta_3$-specific nanoprobe for MRI detection of collaterals. Specifically, Arg-Gly-Asp (RGD) peptides were covalently conjugated on the surface of

Fe_3O_4 nanoparticles, which endowed the nanoparticle with $\alpha_v\beta_3$ integrin targeting capability, thereby visualizing the collateral vessels after onset of acute ischemic stroke. The in vivo SWI results revealed that the collateral vessels quickly formed in the acute phase after the arterial occlusion, but vanished within several hours following the recanalization. This study offers a feasible approach to dynamically monitor the collateral status among different individuals during diagnosis and treatment [84].

In the previous imaging studies, diffusion-weighted imaging (DWI) stands out as a specialized MRI sequence capable of delineating the abnormal water apparent diffusion coefficient (ADC). This technique has been widely used for visualizing the location and extent of the irreversible ischemic core in stroke cases [85–87]. When combined with Fe_3O_4 nanoparticles-based SWI, the intricate processes involved the stroke development can be better reflected. Hou et al. designed a low-immunogenic nanoprobe for acute ischemic stroke precise diagnosis. The self-peptide, a peptide sequence derived from the membrane protein CD47, was conjugated onto the surface of biocompatible Fe_3O_4 nanoparticles as a stealth coating. This modification helps delay macrophage-mediated clearance of the nanoprobes, thereby enhancing their ability to evade the immune system and promoting prolonged circulation in the bloodstream. Through nanoprobe-enhanced SWI, the cerebral microvessels exhibited negative contrast and, more importantly, the spatial distribution of collateral vessels can be clearly delineated. Since the ischemic penumbra is closely related to the collateral circulation, the spatial range of the penumbra can be determined by the distribution patterns of the collateral vessels. Thus, by combining with DWI, the infarct core, the collateral vessels around the infarct core, as well as the range of ischemic penumbra can be readily identified simultaneously (upper panel of Fig. 5) [88]. Very recently, Pan et al. developed a contrast-enhanced SWI technique that employs dextran-modified Fe_3O_4 nanoparticles for high-resolution visualization of collateral circulation and the ischemic penumbra in acute ischemic stroke. These nanoparticles are synthesized via a simple coprecipitation method at room temperature, exhibiting well biocompatibility and a transverse relaxivity of 51.3 mM^{-1} s^{-1} at a 9.4 T magnetic field. Leveraging these MRI properties, the nanoparticle-enhanced SWI allows for detailed, high-resolution imaging of cerebral vessels. When combined with ADC analysis, this imaging approach enables simultaneous mapping of the ischemic core, collateral circulation, and ischemic penumbra [89].

In addition to the stroke diagnosis, the nanoparticle-enhanced SWI technology has been also applied to predict the complications during the stroke treatment. Thrombolytic therapy, which aims at breaking up the thrombus or embolus occluding the cerebral artery, and restoring perfusion to the reversibly ischemic brain tissues, is the dominant strategy to treat the acute ischemic stroke. However, thrombolytic therapy may enhance the risk of hemorrhage transformation (HT) compared to other supportive care. Under this circumstance, the fear of HT largely limits the use of thrombolytic therapy in acute ischemic stroke. Focusing on this dilemma, Gao et al. propose a novel strategy to offer early evidence to predict the possible HT in advance before thrombolytic therapy. The angiogenesis/inflammation dual-targeted MR nanoprobe was constructed by simultaneously connected the c(RGDfC) and angiopep-2 peptides onto the surface of Fe_3O_4 nanoparticles. Such dual-targeted nanoprobes can successfully target the activated vascular endothelial cells and enter the blood–brain barrier (BBB) to anchor on the inflammatory glial cells within HT-risk region via c(RGDfC)/$\alpha_v\beta_3$ and angiopep-2/LRP-1 interaction. Therefore, the range and spatial distribution of abnormal hyperenhancement in SWI following the administration of the nanoprobe can serve as an indicator for the HT risk. This, in turn, provides guidance on the decision to pursue thrombolytic therapy. This endeavor holds significant promise for stroke patients, especially for those who can still benefit from late-stage thrombolytic therapy (lower panel of Fig. 5) [90]. This integrated imaging strategy provides valuable insights into the pathological processes and may contribute to improved diagnostic accuracy in stroke assessment.

Brain tumors, particularly glioblastomas, are among the most aggressive and devastating forms of cancer, often associated with a dismal prognosis. Microangiogenesis, a hallmark of these tumors, is closely linked to the malignancy grade and plays a critical role in tumor progression. In this context, Sun et al. introduced a contrast-enhanced SWI technique that utilizes dextran-modified Fe_3O_4 nanoparticles for ultra-high-resolution vascular mapping in brain tumors. These nanoparticles demonstrate commendable biocompatibility along with a high transverse relaxivity of 159.7 mM^{-1} s^{-1} at a 9.4 T magnetic field. The contrast-enhanced SWI technique enables the visualization of cerebral microvessels as thin as 0.1 mm with exceptional contrast and clarity. This imaging approach allows for detailed observation of both enlarged peritumoral drainage vessels and intratumoral microvessels (Fig. 6). Overall, this study offers a promising method for accurate vascular profiling of brain tumors in clinical setting [91].

Apart from the stoke and cancer evaluation, Fe_3O_4 nanoparticles-based SWI strategy has been also employed to detect other cerebral diseases related to vascular anomalies or dysfunctions. For example, Polymyxin B (PMB), a cationic cyclic polypeptide antibiotic, can exert

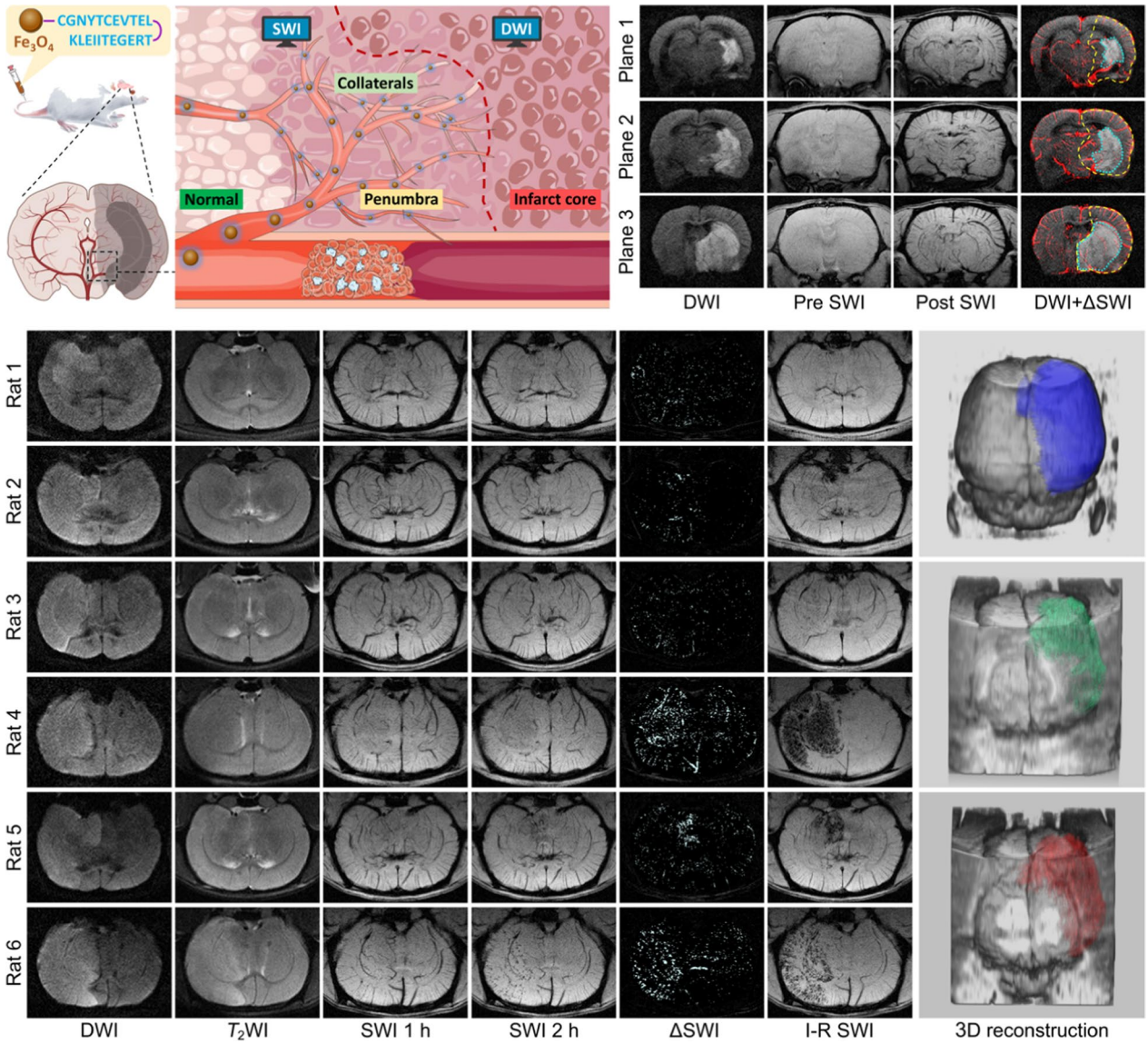

Fig. 5 Schematic illustration for showing the structure of low-immunogenic MRI nanoprobe and the simultaneous identification of infarct core, collaterals and penumbra with nanoprobe-based MRI strategy after the onset of ischemic stroke (upper). MR images of brains of 6 randomly chosen rats underwent rMCAO for different time periods, together with 3D reconstruction according to DWI, pre-reperfusion SWI, and I-R SWI data (from top to bottom), for thrombolytic hemorrhage risk prediction (lower). Reproduced with permission from Hou et al. [88] and Gao et al. [90]

bactericidal effects on multi-resistant Gram-negative bacteria. However, the severe nephrotoxicity and neurotoxicity largely hamper the clinical application of PMB. To accurately evaluate the neurotoxicity in vivo, Zhang et al. employed the biocompatible Fe_3O_4 nanoparticles to noninvasively visualize the potential impairment of Polymyxin B (PMB) to the central nervous system. The Fe_3O_4 nanoparticle-enhanced SWI revealed that the successive PMB injection may lead to the micro-leakage of blood–brain barrier (BBB), indicated by the discrete punctate negative signals distributed asymmetrically within the brain parenchyma. This study offers a feasible strategy for evaluating the central nervous system impairment in real time after the medication of PMB, which is expected to provide guidance for the clinical application of PMB. The real-time assessment achieved in this study establishes a new pathway for the clinical utilization of this conventional antibiotic [74]. In another study, Lan et al. developed a MR molecular imaging approach for depression diagnosis based on inflammation-targeted nanoprobe. The cLABL, a cyclic decapeptide that can specifically bind with ICAM-1 receptor of the inflamed vascular

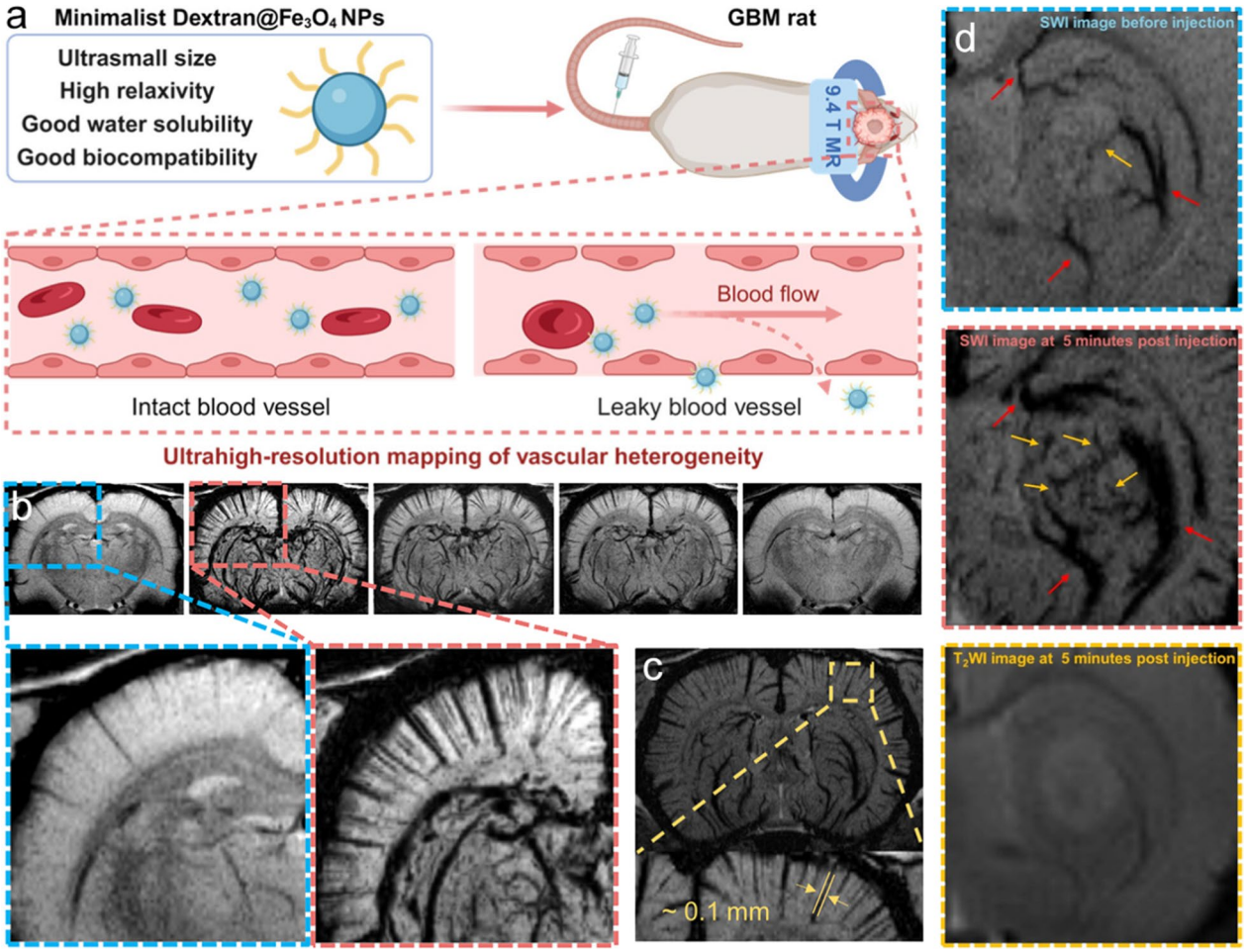

Fig. 6 **a** Schematic illustration of dextran-modified Fe_3O_4 nanoparticles for ultrahigh-resolution vasculature mapping in glioblastomas via the contrast enhanced SWI. **b** The minimum intensity projection images of brain vessels derived from SWI display low signal intensities within a 4.5 mm tissue thickness, projecting them onto the background plane to clearly depict the vascular trajectory. **c** SWI images obtained at 5 min after injection of nanoparticles, with the vascular diameter measurement. **d** MR images of glioblastomas before and after intravenous injection of nanoparticles. The peritumoral drainage vessels and intratumoral microvessels are pointed with red and yellow arrows. Reproduced with permission from Sun et al. [91]

endothelial cells, were conjugated onto the Fe_3O_4 nanoparticles. Following the intravenous administration, the resultant targeted nanoprobe can depicted the cerebral vasculatures and, more importantly, specifically accumulate in the inflammation regions to generate an abnormal enhancement of the SWI signals. Using this strategy, the focal inflammation in some specific brain regions of mice with depression can be visualized noninvasively in vivo [92].

In addition to the laboratory researches, iron oxide nanoparticle-based contrast agent has been introduced into the clinical settings to enhance the sensitivity and resolution of SWI for vascular imaging [93, 94]. Notably, Ferumoxytol, which can be used as an MRA contrast agent as described above, is also the most commonly used contrast agent in human SWI studies [81, 95–97]. Using Ferumoxytol as contrast agent, Haacke et al. and Liu et al. conducted separate investigations on the cerebrovascular imaging at 3 T and 7 T, respectively. Their studies revealed that the resolution of SWI for blood vessels was significantly improved with the increased dose of Ferumoxytol. Through the optimization of the imaging parameters, they achieved successful detection of vessels with diameters as low as 50 μm (Fig. 7) [81, 98]. These studies strongly demonstrated the microvascular imaging capability of Ferumoxytol-enhanced SWI. Therefore, the utilization of iron oxide nanoparticles as contrast agents presents an opportunity to visualize the sophisticated microvascular systems. This method holds significant potential for the diagnosis of various diseases that are associated with the microvasculatures, especially the cerebral diseases.

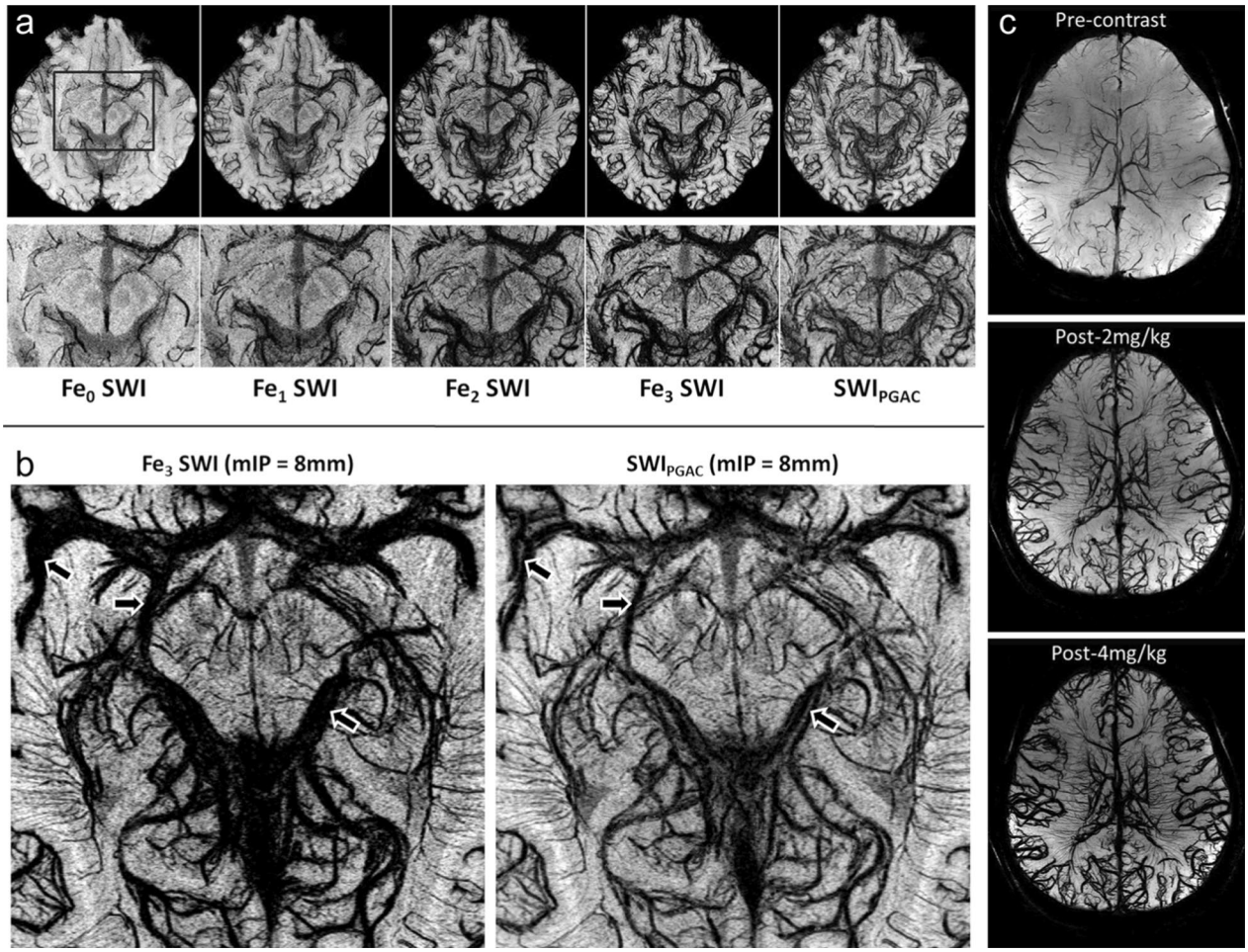

Fig. 7 Microvasculature SWI of the midbrain enhanced by Ferumoxytol. **a** Pre-contrast (Fe_0), post-contrast SWI data (Fe_1, Fe_2, Fe_3) as well as the SWI_{PGAC} obtain at 3 T are shown in the top row, whereas the bottom row shows their corresponding zoomed insets, focusing on the midbrain region **b**. **c** Visualization of arteries and veins using minimum intensity projections of SWI at 7 T with different doses of Ferumoxytol. Reproduced with permission from Haacke et al. [81] and Liu et al. [98]

In addition to iron oxide nanoparticle-based contrast agents, recent studies have demonstrated that $NaGdF_4$ nanoparticles can also enhance SWI contrast. This effect is attributed to the regular arrangement of Gd^{3+} ions within the crystal lattice, which induces magnetic anisotropy, generating local static magnetic field heterogeneity and resulting in negative signals in T_2-weighted sequences. Consequently, $NaGdF_4$ nanoparticles serve as versatile MRI contrast agents, enabling multimodal vascular imaging. Specifically, vessels can be brightened in the CE MRA sequence and darkened in the SWI sequence, facilitating better differentiation of fine vascular structures. Building on this principle, Hou et al. utilized PEGylated $NaGdF_4$ as a contrast agent to achieve high-resolution, multiparametric MR vascular imaging. In particular, tiny vessel branches as thin as 150 μm in diameter can be clearly distinguished in 3D CE MRA, while even smaller microvessels with the size of *ca.* 60 μm in diameter, can be visualized using SWI. This enhanced vascular imaging resolution allows for precise in vivo diagnosis of various vascular diseases, including Alzheimer's disease and ischemic stroke, in rodent models. Furthermore, dual-contrast imaging was successfully demonstrated in swine using a clinical 3.0 T human MRI scanner, underscoring the promising clinical translation potential of this imaging approach [99].

Superficial vascular imaging with NIR-II fluorescence imaging

In addition to MRA and SWI, fluorescence-based optical imaging technologies, known for their capacity for noninvasiveness procedures, high sensitivity, real-time feedback, have found extensive applications in the field

of bioimaging [100–102]. Contrasted with the visible and NIR-I imaging windows (400–900 nm) which often hindered by the light absorption, light scattering and autofluorescence within biological tissues, the NIR-II imaging window (1000–1700 nm) has proven effective for achieving high-resolution imaging at tissue depths in the centimeter range. This success can be attributed to the suppression of photon scattering and the decreasing of tissue autofluorescence within this specific spectral range [103–106]. As a result, NIR-II fluorescence imaging showcase greater potential in the context of vascular imaging.

To date, a rage of NIR-II imaging probes have been developed to facilitate the vascular imaging. Among these, small-molecule dyes offer high quantum yields and strong NIR absorbance but are hindered by low solubility, rapid clearance, and systemic toxicity, limiting their practical applications [107, 108]. In recent years, the advancement of nanotechnology has provided promising solutions to these challenges. The incorporation of nanocarriers can improve the water solubility and circulation time of these small-molecule dyes, while certain nanomaterials can intrinsically emit NIR signals, serving as natural NIR imaging agents. Notably, multifunctional nanoprobes—basing on quantum dots, rare-earth doped down-conversion nanoparticles, or single-walled carbon nanotubes (SWNTs)—have been developed, offering versatile options for realizing NIR-II vascular imaging [1, 109, 110]. Similar to MRI-based vascular imaging, NIR-II vascular imaging benefits from the larger hydrodynamic diameters of nanosized imaging agents, which help extend circulation time and provide a broader imaging window compared with small-molecule probes that tend to leak rapidly from the vasculature. Over the past decade, NIR-II vascular imaging approaches using nanomaterials as imaging agents have been widely exploited to depict the superficial vasculatures in vivo. In 2012, Dai et al. employed fluorescent SWNTs as imaging agents to conduce the real-time NIR vascular imaging of mouse hind limb. The small vessels at depths ranging from 1 to 3 mm can be imaged with high spatial resolution (~30 μm) and temporal resolution (< 200 ms per frame). Moreover, the application of a dynamic contrast-enhanced NIR-II imaging technique allowed for clear differentiation between arterial and venous vessels [110]. In the subsequent study, Huang et al. employed the PbS@CdS quantum dots (QDs) as the imaging agents to visualize the vascular anatomical structures and quantify the vascular hemodynamics of mice with peripheral arterial diseases. Notably, through using this QDs-based NIR-II imaging strategy, the vascular occlusion, revascularization, and compensatory angiogenesis in the ischemic limb was clearly observed [111]. Near recently, Zhu et al. prepared lanthanide-doped core–shell–shell nanoparticles β-$NaErF_4$: 2%Ce@$NaYbF_4$@$NaYF_4$ with relatively high photoluminescence quantum yield in aqueous solution (9.2%). The PL lifetime at 1525 nm is tunable through regulating the thickness of $NaYF_4$ layers. Benefiting from these properties, the nanoparticles were subsequently employed as imaging agents for NIR-II fluorescence lifetime vascular imaging. By using a lifetime imaging system, the superficial vascular network in murine abdomen can be successfully displayed [112].

In addition to blood vessels in the superficial trunk and limbs, the structure of blood vessels in the cerebral cortex can also be clearly presented through nanomaterial-enhanced NIR-II fluorescence imaging. For example, Dai et al. prepared rare-earth Er-based nanoparticles to facilitate the quick imaging (20 ms exposure time per frame) of cerebral vessels in mice with high spatiotemporal resolution within NIR-IIb window (1500 nm~1700 nm) [113]. In another study, using polyacrylic acid (PAA) modified $NaYF_4$:Gd/Yb/Er nanorods as the contrast agent, Hao et al. acquired the noninvasive cerebral vascular imaging through scalp and skull without craniotomy, in which the microvessels as thin as 43.65 μm can be clearly distinguished [114]. Very recently, Wu et al. found that the introduction of a rigid conjugated polymer can induce the chain packing of the NIR-II semiconducting polymers, resulting in the formation of spherical Pdots with compact structures, narrow size distribution, and bright NIR-II emission (Fig. 8a). These Pdots can be employed as fluorescent agent for vascular imaging in living animals. Furthermore, by leveraging a vessel segmentation strategy based on Hessian matrix, the tubular structures in the NIR fluorescence imaging could be identified and extracted. This approach led to a significant improvement in the vascular contrast of angiograms, achieving a 13-fold improvement in signal -to-background ratio as compared to the original images (Fig. 8b). Combining the merits of Pdots and the Hessian matrix strategy, the high-contrast cerebral angiograms of mouse and rat models bearing brain tumors can be acquired in through-skull NIR-II imaging, in which the tumor-associated twisted and disorganized vasculature can be clearly observed (Fig. 8c) [115].

In the terms of tumor diagnosis, NIR vascular imaging provides innovative perspectives. Li et al. prepared $NaYF_4$:Nd@$NaGdF_4$ nanoparticles as imaging agents. Using NIR-II imaging, the temporal evolution of angiogenesis during the development of orthotopic breast tumor in mice were successfully obtained. This imaging strategy facilitates a comprehension of tumor progression and staging through the analysis of vascular variations [116]. In subsequent studies, Gao et al. designed and prepared the $NaErF_4$@$NaYbF_4$@$NaYF_4$ nanocrystals with

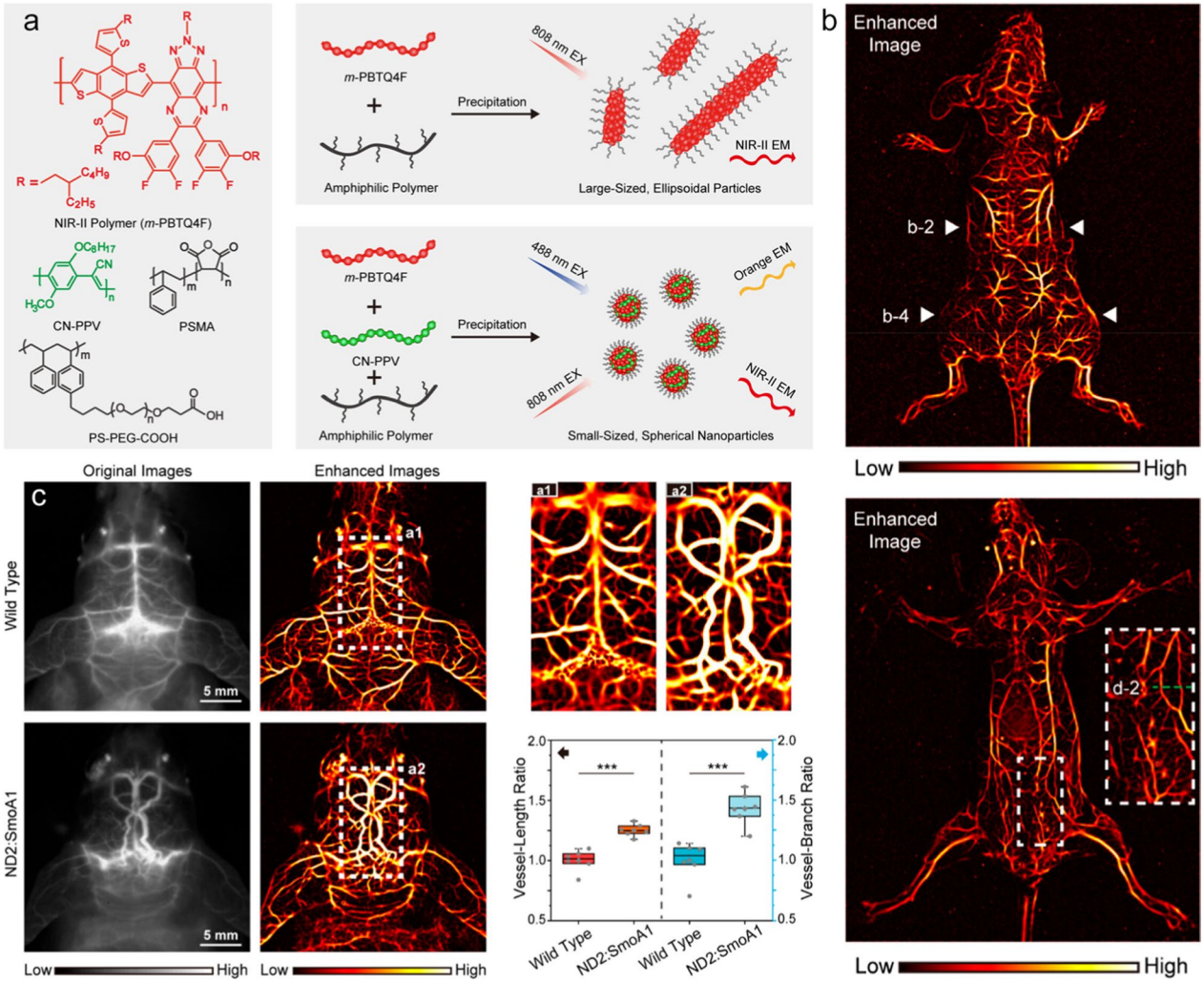

Fig. 8 **a** Molecular structures of NIR-II polymer (m-PBTQ4F), short-rigid polymer (CN-PPV), and amphiphilic polymer (PSMA and PS-PEG-COOH), and the preparation and morphology modulation of NIR-II Pdots by blending amphiphilic polymer and short-rigid polymer during preparation. **b** NIR-II fluorescence image of a mouse acquired in prostrate and supine. **c** In vivo NIR-II fluorescence images of cerebral vasculature of mice with an intact skull and scalp, together with the quantitative comparison of vessel-length and vessel-branch in the cerebral vasculature between wild-type and tumor-bearing mice by using vascular segmentation and quantification algorithm. Reproduced with permission from Wu et al. [115]

core/shell/shell structures, which exhibited both upconversion and down-conversion NIR-II emissions. Upon intravenous injection, the nanocrystals exhibited the ability to brighten the superficial vasculatures in the abdomen of mice. The blood supply to the < 3 mm tiny tumor located in the peritoneum of mice can be clearly observed [117]. Very recently, Zhong et al. developed a nanoparticle-based vascular imaging strategy to dynamically monitor the intracapillary oxyhemoglobin saturation (sO_2). They prepared the $NaErF_4$@$NaYF_4$ nanoparticles that can generate NIR-IIb luminescence at 1550 nm under multiple excitation wavelengths at 650 nm, 808 nm and 980 nm. Owing to the absorption difference between oxyhaemoglobin (HbO_2) and deoxyhaemoglobin (HbR) in the spectral range of 600–1000 nm, the ratio of emission intensity of nanoparticles under the excitation of 650 nm and 980 nm can be used to quantitatively visualize the relative content of HbO_2 and HbR in the blood samples (Fig. 9a–e). By leveraging this strategy, the sO_2 levels in tumor-related vasculatures were demonstrated to be closely correlated with O_2 consumption of cancer cells (Fig. 9f–i). Additionally, the reduction of sO_2 level within tumor vessels could also serve as an indicator of a positive response to tumor immunotherapy [118].

Apart from the disease diagnosis, NIR-II vascular imaging can also contribute to the intraoperative navigation with quick acquisition and high precision. For example, the flap perfusion status decides the survival

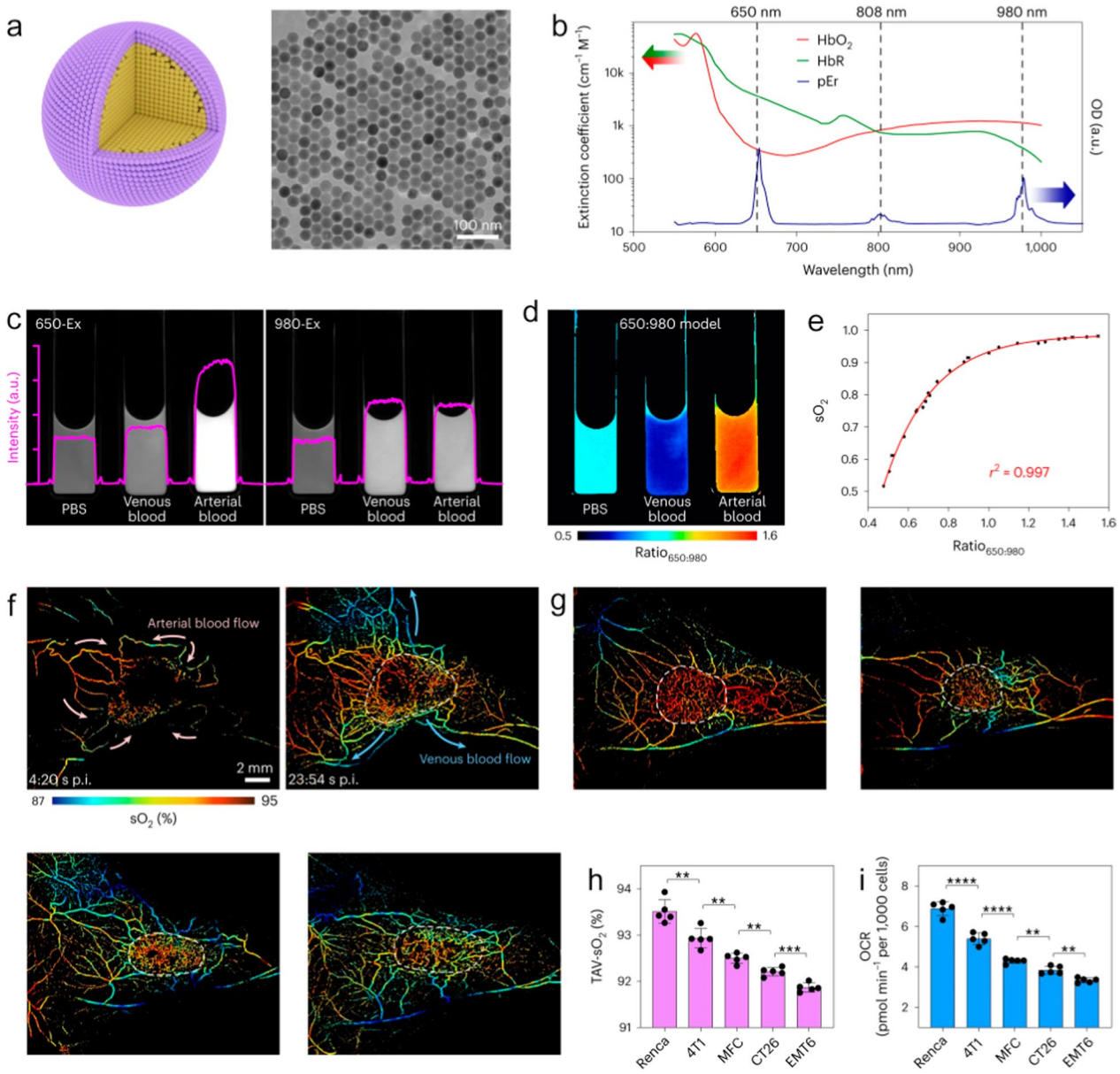

Fig. 9 **a** Schematic illustration of a core–shell $NaErF_4$@$NaYF_4$ pEr nanoprobe (left) and corresponding large-scale transmission electron microscopy image (right). **b** Absorption spectra of HbO_2, HbR and pEr. **c** NIR-IIb luminescence images of the pEr nanoprobe dispersed in PBS, mouse venous blood and arterial blood under 650-Ex and 980-Ex. **d** Heat map of the $ratio_{650:980}$ reconstructed from the 650-Ex and 980-Ex channels. **e** The sO_2 value of mouse blood samples, as measured by a blood-gas analyser, was plotted against the $ratio_{650:980}$ to generate an empirical calibration formula. **f** Time-course dynamic sO_2 imaging (650: 980 model) showing the perfusion of pEr into 4T1 tumor. The pink (left) and azure (right) arrows indicate the blood flow directions. **g** NIR-II sO_2 imaging showed the tumor-associated vasculature of different tumors. **h** Statistical results of the average TAV-sO_2 values within the tumor regions. **i** Basal oxygen consumption rate of these five types of cancer cell lines. Reproduced with permission from Zhong et al. [118]

opportunity of the translated flap and surgical prognosis. The monitoring of the revascularization during the surgery and the angiogenesis after surgery are very crucial for the evaluation of the prognosis and clinical outcome of the flap transplantation. Chen et al. proposed a QD-based NIR-II vascular imaging approach to dynamically evaluate the perfusion status of transplanted flap intra- and post-operatively. By leveraging the high-resolution vascular imaging enhanced by Ribonuclease-A-coated PbS/ZnS QDs, the microvasculature structures and the blood perfusion status of the perforator flap could be visualized during and at different time points within

2 weeks after surgery, allowing for the precise assessment of necrosis and survival regions of the transplanted skin flap [119]. In addition to the flap transplantation, the NIR-II vascular imaging technique can also be used to evaluate the outcome of organ transplantation. Tang et al. employed a NIR-II fluorescence imaging technology to evaluate the blood reperfusion of donor kidney and monitor the vascular anastomosis and ureterovesical connection after the organ transplantation surgery, in which aggregation-induced emission (AIE) active NIR-II DIPT-ICF nanoparticles were synthesized as imaging agents. Benefiting from the long blood circulation time, a single injection of DIPT-ICF nanoparticles could realize the whole-process monitoring and evaluation of renal transplantation. Such imaging strategy offers a practical method to prevent injury during nephrectomy, safeguard donor kidney quality, and assess renovascular reconstruction through renal angiography, which will largely improve the survival rate of the transplanted kidney while minimizing the undesired complications (Fig. 10)

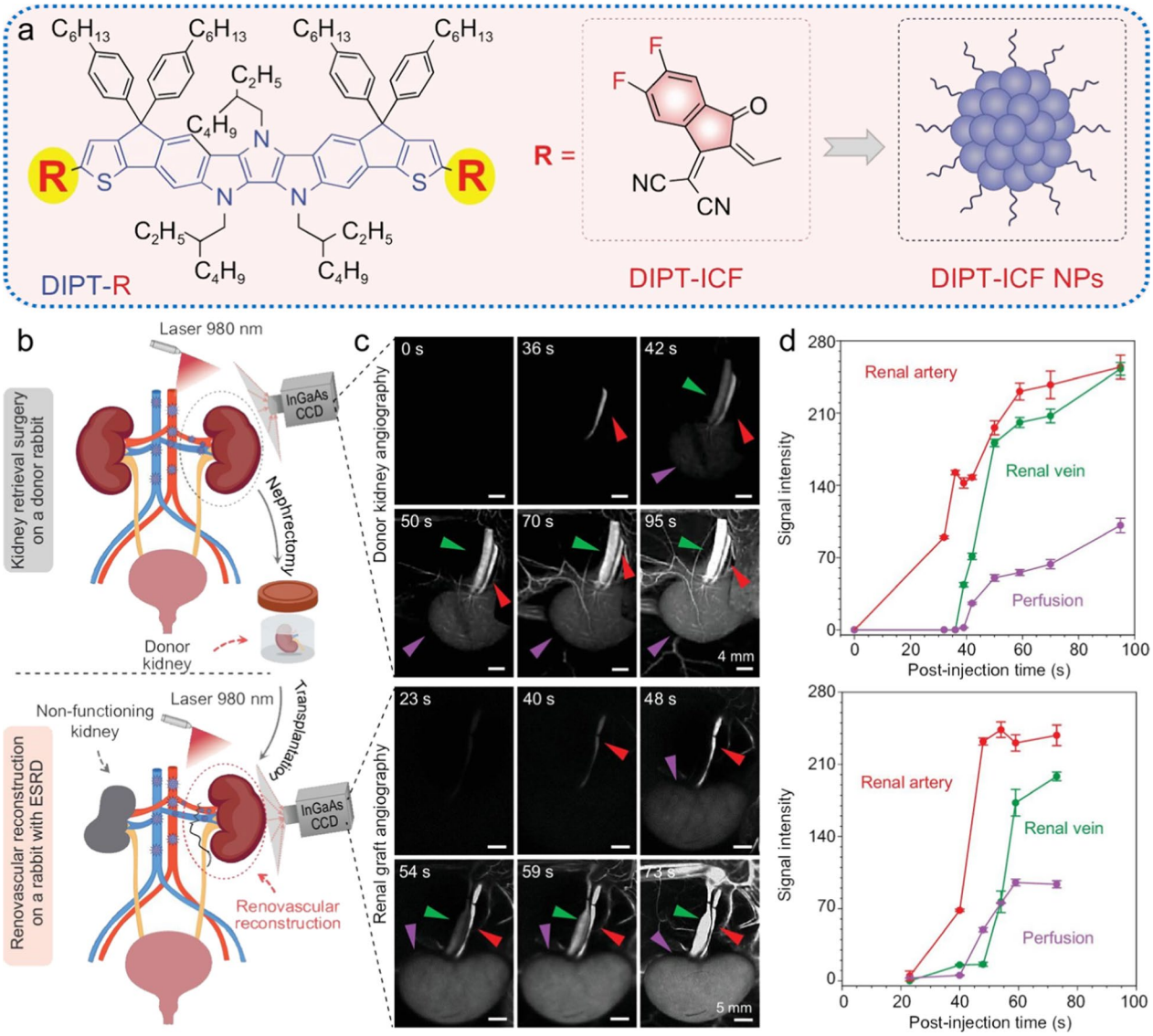

Fig. 10 **a** Schematic illustration of the chemical structures of DIPT-IC and DIPT-ICF nanoparticles. **b**–**d** Renal angiography of donor and recipient rabbits in the NIR-II window based on DIPT-ICF NPs during kidney retrieval and implantation. **b** Schematic illustrations of the donor kidney retrieval surgery (upper)/kidney implantation surgery (lower) and renal angiography. **c** NIR-II images of renal arteries, renal veins and donor kidneys (upper)/graft arteries, veins and graft reperfusion following renal vessel anastomosis at different time points after intravenous injection of DIPT-ICF NPs. **d** Quantitative analysis of NIR-II fluorescence intensity of kidneys and their accessory vessels. Red arrows, green arrows and purple arrows represent renal arteries, renal veins and kidneys. Reproduced with permission from Tang et al. [120]

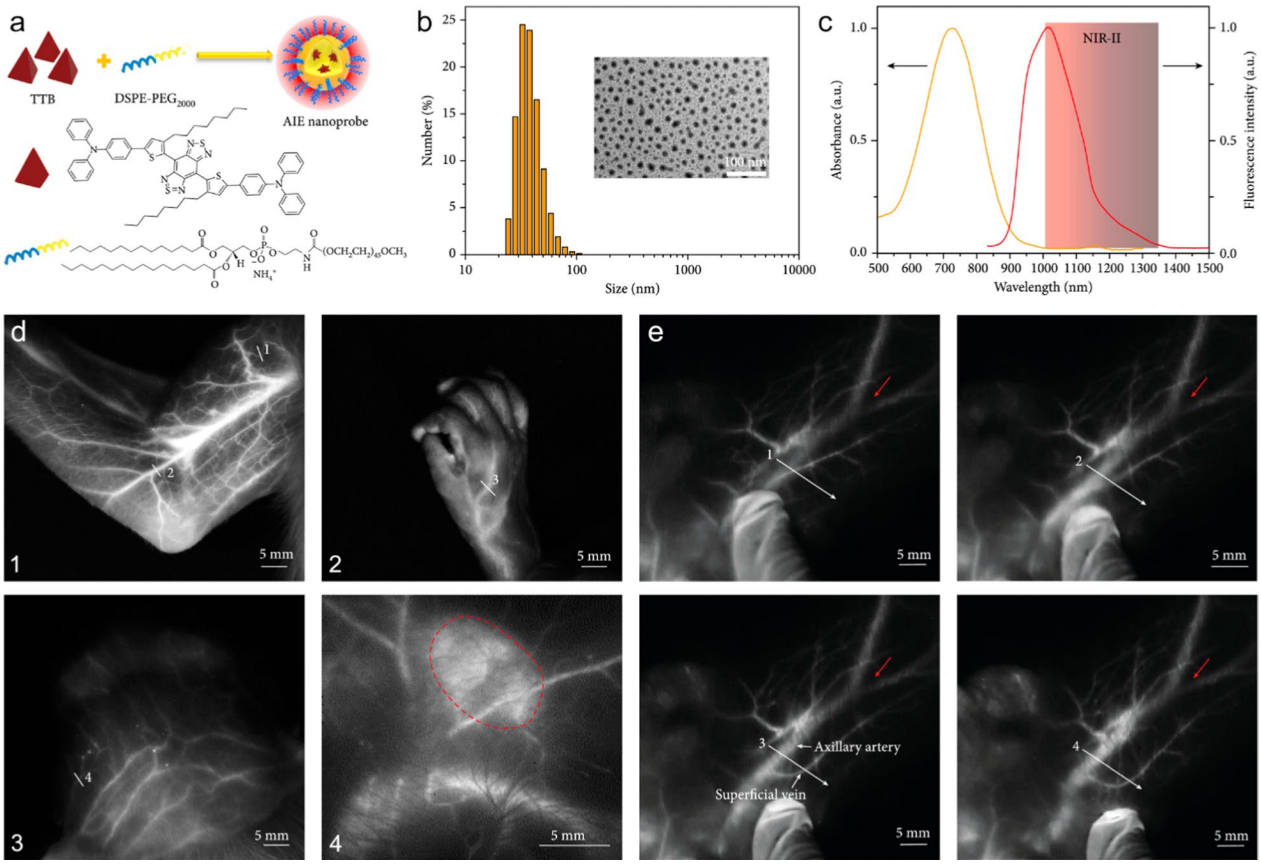

Fig. 11 **a** The preparation of AIE probes via a nanoprecipitation method. **b** Dynamic light scattering data of aqueous AIE probes. Inset: transmission electron microscopy image of water-dispersed AIE probes. **c** Fluorescence and absorption spectra of AIE probes. **d** NIR-II fluorescence imaging of the vessels and lymph nodes in cynomolgus monkey after intravenous injection of the AIE probes. (1) arm, (2) hand, (3) scalp vasculature, (4) an axillary lymph node marked by the red dotted line. **e** NIR-II fluorescence imaging of the deep axillary artery in a healthy adult cynomolgus monkey after intravenous injection of AIE probes. When epidermis was moved, the superficial vein was moved accordingly; however, the deep axillary artery remained stationary. Reproduced with permission from Tang et al. [121]

[120]. The above studies highlighted the remarkable spatial and temporal resolution achieved by the nanomaterials-enhanced NIR-II vascular imaging. Nevertheless, the lack of data from large animal experiments hinders the process of clinical translation of these innovative strategies. Addressing this issue, Tang et al. conducted a study validating the feasibility of AIE nanoprobe-based NIR-II imaging strategy on three cynomolgus monkeys. This research focused on evaluating the imaging performance and biosafety features of the AIE nanoprobe on nonhuman primate models. The results revealed that the arterial structures at a depth of 1.5 cm within the monkey tissue can be depicted with high contrast and resolution, which elevate the fluorescence imaging depth from millimeter to centimeter level (Fig. 11). In addition, the intravenously administration of AIE nanoprobe does not lead to obvious adverse side effects, supported by hematological and tissue analysis. This study not only showcases the clinical translational potential of the prepared AIE nanoprobes, but also confirms the viability of the clinical translation process for the nanoprobe-enhanced NIR-II vascular imaging approach [121].

Summary and outlook

Advantages and limitations of nanotechnology-based vascular imaging approaches

In this review, the state-of-art of nanotechnology-based vascular imaging strategies crossing different imaging modalities have been summarized by giving corresponding examples. Specifically, NIR-II vascular fluorescence imaging presents the highest sensitivity and quick feedback, in which the blood vessels with the diameter of less than 30 μm can be distinguished. However, while nanomaterial-based NIR-II fluorescence imaging successfully facilitates real-time visualization of superficial vascular structures, it is important to note that this imaging modality is still constrained by its inherent limitations regarding tissue penetration depth. Compared to

fluorescence imaging, nanomaterials-based MRI allows for the observation of deep-seated blood vessels inside tissues, which demonstrates a broader range of applicability in disease detection. In particular, by leveraging the nanomaterial-enhanced MRA, the 3D anatomical structures of the sophisticated vasculatures, including the different small branches of arteries and veins down to ~100 μm, and abnormal morphological variations, can be rapidly outlined. This imaging modal provides comprehensive spatial distribution information of the vascular systems. In addition to 3D MRA, nanomaterial-enhanced SWI allows for the precise depiction of micro-vessels with a resolution of less than 50 μm. This is achieved through its heightened sensitivity to the magnetic susceptibility of various tissues, resulting in remarkably enhanced contrast. Owing to the intrinsic magnetic susceptibility of different tissues, the enhanced SWI not only enables the mapping of vasculatures, but also achieves higher resolution in visualizing surrounding tissues. Therefore, SWI offers valuable insights into the intricate relationship between vascular abnormalities and adjacent tissues, which has been proved particularly well-suited for the visualization of cerebrovascular-related disorders, such as collaterals formation and cerebral micro-hemorrhage. Nevertheless, these two MRI modalities still face limitations such as long scanning and post-processing times, as well as challenges in assessing vascular hemodynamics.

Due to the inherent clinical compatibility of MR imaging modality, nanomaterial-based contrast agents for MR vascular imaging have been successfully applied in practical clinical settings. This is particularly evident in vascular imaging involving special patient populations, including the elderly, young children, and individuals with renal insufficiency. These applications reveal distinctive potential, highlighting the efficacy and versatility of such agents in enhancing diagnostic imaging outcomes. In comparison, the utilization of NIR vascular imaging in clinical diagnosis remains constrained mainly due to the insufficient proliferation of fluorescence imaging modality, lack of standardization, inadequate clinical validation, and the challenges in imaging resolution and tissue penetration. While fluorescence imaging is hindered by these limitations, its high sensitivity, quick feedback property, cost-effectiveness, and the portability of equipment distinguish it favorably from other imaging modalities. These distinctive advantages endow the NIR fluorescence vascular imaging with substantial potential in specific clinical scenarios, such as the monitoring of blood perfusion post-skin flap or organ transplantation, as well as real-time navigation during intraoperative revascularization. Currently, numerous researchers are dedicated to advancing the optical imaging devices and promoting the application of NIR vascular imaging in clinical practice. In 2019, Tian et al. developed an optical-imaging device that combines visible and NIR fluorescence for human use. With this device, the surgical resection of liver tumor in 23 patients were successfully guided by detecting the NIR fluorescence from indocyanine green (ICG). This study demonstrated the potential of NIR fluorescence imaging in clinical settings, advancing its use in medical practice [122]. In the subsequent years, they also realize the accurate resection of hepatic carcinoma, glioma, and cystic renal masses in different human patients [123–125]. In 2022, Cheng et al. utilized the portable NIR-II imaging with ICG as an operative evaluation tool to improve the operation efficiency in microsurgery of 39 patients who undergoing microvascular anastomosis, digit replantation, avulsion injury or perforator-based island flap surgery. Through using ICG-enhanced NIR-II imaging, the anastomotic vessels can be rapidly visualized, ensuring the preservation of the salvaged distal limbs. Overall, this imaging strategy facilitated the identification of perforator vessels and the estimation of perforator areas before obtaining the flap, which offered useful information for prognosis assessment of microsurgery [126]. Building on these clinical studies, it is anticipated that with the increasing availability of medical fluorescence imaging devices and ongoing research on the design of nanomaterial imaging agents, nanomaterial-based NIR fluorescence vascular imaging will find extensive application in monitoring various related-diseases.

Considering the unique advantages and diverse clinical applications of the imaging modalities discussed, the integrated use of multiple vascular imaging techniques is likely to emerge as a future trend. This approach has already demonstrated significant promise in tumor imaging, where it has enhanced the precision and comprehensiveness of diagnoses. For instance, previous studies have developed various nanoprobes to enable multimodal cancer diagnosis in laboratory settings [127–129]. Given the advancements in multimodal imaging technologies and their successful applications in oncology, it is reasonable to anticipate that similar strategies could be adapted for vascular imaging. By integrating these techniques, vascular imaging could benefit from complementary information, ultimately improving the accuracy and effectiveness of the diagnostic process.

Challenges in the clinical translation of nanotechnology for vascular imaging

Despite the significant advantages, several issues in terms of clinical translation still need to be carefully considered for nanomaterial-based vascular imaging. The physicochemical properties of nanomaterials, such

as size, rigidity, and surface structure, play pivotal roles in determining their pharmacokinetics. Previous studies indicated that nanomaterials smaller than 6.5 nm can pass the glomerular filtration, primarily eliminating through the urinary system [130–132]. This pharmacokinetic profile mitigates the potential long-term side effects associated with body accumulation of nanomaterials. However, the rapid renal clearance will lead to the short blood circulation time, consequently narrowing the time window for vascular imaging. Hence, achieving a delicate balance between blood circulation time and renal clearance is imperative. Alternatively, nanomaterials with sizes exceeding the glomerular filtration limit may be recognized and taken up by the mononuclear phagocytic system, leading to their long-term accumulation in the liver or spleen. If the mononuclear phagocytic system can be bypassed, the nanoparticles may undergo hepatobiliary elimination and be excreted from the body via feces [133, 134]. These pharmacokinetic routes do not require kidney involvement, rendering it applicable to vascular imaging in patients with renal insufficiency. Nevertheless, in such scenarios, careful evaluation is essential to assess whether the prolonged retention of the nanomaterials in the liver and spleen lead to the undesired adverse side effects. Overall, when designing nanomaterials as vascular imaging agents, it is crucial not only to focus on the vascular imaging performances, but also to carefully consider the pharmacokinetics, along with the corresponding clinical indications.

In addition to achieving an optimal balance between imaging performance and pharmacokinetics, a significant challenge in the clinical translation of nanomaterials is scaling up their production from the laboratory settings to industrial manufacturing. The complex chemical and physicochemical processes involved in nanomaterial synthesis make it challenging to maintain both quality and imaging performance during large-scale production. Addressing these issues is essential for the successful clinical application and widespread use of nanomaterials.

To sum up, there is high anticipation that nanomaterial-based vascular imaging strategy could play an important role in the future clinical diagnosis for patients with vascular-related diseases. This could lead to the development of personalized treatment strategies for individuals, marking an update in the diagnostic paradigm.

Author contributions

P. Zhang proposed the conceptual framework and authored the review under the guidance of Y. Hou and X. Luo. Y. Li, X. Li and Y. Wang helped organize the review and prepare the manuscript. H. Lin and N. Zhang participated in the discussion of the clinical imaging section. M. Jiao, W. Li and L. Jing review the manuscript and engaged in scholarly discussions. All authors provided critical conceptual input and critically revised the review.

Funding and acknowledgements

The authors thank the financial support from National Natural Science Foundation of China (82102679, 22177009, 22174082, 22374085, 22177115), the Natural Science Foundation of Shandong Province of China (ZR2023MB057), and the Youth Innovation Promotion Association CAS (Y2022017).

Availability of data and materials

No datasets were generated or analysed during the current study.

Declarations

Ethics approval and consent to participate

Not applicable.

Consent for publication

We give our consent for the manuscript to be published in Journal of Nanobiotechnology.

Competing interests

The authors declare no competing interests.

Author details

[1]Key Laboratory of Optic-Electric Sensing and Analytical Chemistry for Life Science, MOE, College of Chemistry and Molecular Engineering, Qingdao University of Science and Technology, Qingdao 266042, China. [2]College of Life Science and Technology, Beijing University of Chemical Technology, Beijing 100029, China. [3]Department of Psychiatry, West China Hospital of Sichuan University, Chengdu 610041, China. [4]Beijing National Laboratory for Molecular Sciences, CAS Key Laboratory of Colloid and Interface and Thermodynamics, CAS Research/Education Center for Excellence in Molecular Sciences, Center for Carbon Neutral Chemistry, Institute of Chemistry, Chinese Academy of Sciences, Bei Yi Jie 2, Zhong Guan Cun, Beijing 100190, China.

Received: 7 March 2024 Accepted: 28 November 2024
Published online: 18 December 2024

References

1. Wang ZA, Wang X, Wan JB, et al. Optical imaging in the second near infrared window for vascular bioimaging. Small. 2021;17:2103780.
2. Holmstedt CA, Turan TN, Chimowitz MI. Atherosclerotic intracranial arterial stenosis: risk factors, diagnosis, and treatment. Lancet Neurol. 2013;12:1106–14.
3. Xie G, Lin S, Wu F, et al. Nanomaterial-based ophthalmic drug delivery. Adv Drug Delivery Rev. 2023;200:115004.
4. Qiao R, Huang X, Qin Y, et al. Recent advances in molecular imaging of atherosclerotic plaques and thrombosis. Nanoscale. 2020;12:8040–64.
5. Lindsey ML, Bolli R, Canty JM, et al. Guidelines for experimental models of myocardial ischemia and infarction. Am J Physiol Heart Circ Physiol. 2018;314:H812–38.
6. Balami JS, White PM, McMeekin PJ, et al. Complications of endovascular treatment for acute ischemic stroke: prevention and management. Int J Stroke. 2017;13:348–61.
7. Dvorak HF. Tumor stroma, tumor blood vessels, and antiangiogenesis therapy. Cancer J. 2015;21:237–43.
8. Chen F, Cai W. Tumor vasculature targeting: a generally applicable approach for functionalized nanomaterials. Small. 2014;10:1887–93.
9. He P. Leucocyte/endothelium interactions and microvessel permeability: coupled or uncoupled? Cardiovasc Res. 2010;87:281–90.
10. Barlinn K, Alexandrov AV. Vascular imaging in stroke: comparative analysis. Neurotherapeutics. 2011;8:340–8.
11. Murphy DJ, Aghayev A, Steigner ML. Vascular CT and MRI: a practical guide to imaging protocols. Insights Imaging. 2018;9:215–36.
12. Demarin V, Morovic S, Korczyn AD. Ultrasound subclinical markers in assessing vascular changes in cognitive decline and dementia. J Alzheimer's Dis. 2014;42:S259–66.

13. Terkawi AS, Karakitsos D, Elbarbary M, et al. Ultrasound for the anesthesiologists: present and future. Sci World J. 2013;2013:1–15.
14. Hargreaves B. Rapid gradient-echo imaging. J Magn Reson Imaging. 2012;36:1300–13.
15. Hallouard F, Anton N, Choquet P, et al. Iodinated blood pool contrast media for preclinical X-ray imaging applications-a review. Biomaterials. 2010;31:6249–68.
16. Wunder A, Klohs J. Optical imaging of vascular pathophysiology. Basic Res Cardiol. 2008;103:182–90.
17. Jiang Y, Pu K. Molecular fluorescence and photoacoustic imaging in the second near-infrared optical window using organic contrast agents. Adv Biosyst. 2018;2:1700262.
18. Tsapis N. Agents de contraste pour l'imagerie médicale. Méd Sci. 2017;33:18–24.
19. Wallyn J, Anton N, Akram S, et al. Biomedical imaging: principles, technologies, clinical aspects, contrast agents, limitations and future trends in nanomedicines. Pharm Res. 2019;36:78.
20. Soufi GJ, Hekmatnia A, Iravani S, et al. Nanoscale contrast agents for magnetic resonance imaging: a review. ACS Appl Nano Mater. 2022;5:10151–66.
21. Jiang Z, Zhang M, Li P, et al. Nanomaterial-based CT contrast agents and their applications in image-guided therapy. Theranostics. 2023;13:483–509.
22. Li J, Centurion F, Chen R, et al. Intravascular imaging of atherosclerosis by using engineered nanoparticles. Biosensors. 2023;13:319.
23. Li Y, Younis MH, Wang H, et al. Spectral computed tomography with inorganic nanomaterials: state-of-the-art. Adv Drug Delivery Rev. 2022;189:114524.
24. Simionescu M, Gafencu A, Antohe F. Transcytosis of plasma macromolecules in endothelial cells: a cell biological survey. Microsc Res Tech. 2002;57:269–88.
25. Zhang P, Li Y, Tang W, et al. Theranostic nanoparticles with disease-specific administration strategies. Nano Today. 2022;42:101335.
26. Zhang P, Wang Z, Wang Y, et al. An MRI contrast agent based on a zwitterionic metal-chelating polymer for hepatorenal angiography and tumor imaging. J Mater Chem B. 2020;8:6956–63.
27. Grover VPB, Tognarelli JM, Crossey MME, et al. Magnetic resonance imaging: principles and techniques: lessons for clinicians. J Clin Exp Hepatol. 2015;5:246–55.
28. Chen C, Ge J, Gao Y, et al. Ultrasmall superparamagnetic iron oxide nanoparticles: a next generation contrast agent for magnetic resonance imaging. WIREs Nanomed Nanobi. 2021;14:e1740.
29. Zhang H, Liu XL, Fan HM. Advances in magnetic nanoparticle-based magnetic resonance imaging contrast agents. Nano Res. 2023;16:12531–42.
30. Ni D, Bu W, Ehlerding EB, et al. Engineering of inorganic nanoparticles as magnetic resonance imaging contrast agents. Chem Soc Rev. 2017;46:7438–68.
31. Miyazaki M, Isoda H. Non-contrast-enhanced MR angiography of the abdomen. Eur J Radiol. 2011;80:9–23.
32. Özsarlak Ö, Van Goethem JW, Maes M, et al. MR angiography of the intracranial vessels: technical aspects and clinical applications. Neuroradiology. 2004;46:955–72.
33. Wilson GJ, Maki JH. Non-contrast-enhanced MR imaging of renal artery stenosis at 1.5 Tesla. Magn Reson Imaging Clin N Am. 2009;17:13–27.
34. Krings T, Hans F-J, Möller-Hartmann W, et al. Time-of-flight-, phase contrast and contrast enhanced magnetic resonance angiography for pre-interventional determination of aneurysm size, configuration, and neck morphology in an aneurysm model in rabbits. Neurosci Lett. 2002;326:46–50.
35. Potthast S, Maki JH. Non-contrast-enhanced MR imaging of the renal arteries. Magn Reson Imaging Clin N Am. 2008;16:573–84.
36. Ivancevic MK, Geerts L, Weadock WJ, et al. Technical principles of MR angiography methods. Magn Reson Imaging Clin N Am. 2009;17:1–11.
37. Hartung MP, Grist TM, François CJ. Magnetic resonance angiography: current status and future directions. J Cardiovasc Magn Reson. 2011;13:19.
38. Caravan P, Ellison JJ, McMurry TJ, et al. Gadolinium(III) chelates as MRI contrast agents: structure, dynamics, and applications. Chem Rev. 1999;99:2293–352.
39. Scott LJ. Gadobutrol: a review of its use for contrast-enhanced magnetic resonance imaging in adults and children. Clin Drug Investig. 2013;33:303–14.
40. Scott LJ. Gadobutrol: a review in contrast-enhanced MRI and MRA. Clin Drug Investig. 2018;38:773–84.
41. Ananta JS, Godin B, Sethi R, et al. Geometrical confinement of gadolinium-based contrast agents in nanoporous particles enhances T1 contrast. Nat Nanotechnol. 2010;5:815–21.
42. Lin YH, Hwang RM, Chen BB, et al. Vascular and hepatic enhancements at MR imaging: comparison of Gd-EOB-DTPA and Gd-DTPA in the same subjects. Clin Imaging. 2014;38:287–91.
43. Peldschus K, Hamdorf M, Robert P, et al. Comparison of the high relaxivity Gd chelates P1152 and Gd-BOPTA for contrast-enhanced MR angiography in rabbits at 1.5 Tesla and 3.0 Tesla. J Magn Reson Imaging. 2010;32:459–65.
44. Li H, Luo Q, Zhu H, et al. An advanced micelle-based biodegradable HPMA polymer-gadolinium contrast agent for MR imaging of murine vasculatures and tumors. Polym Chem-UK. 2020;11:6374–86.
45. Zhang P, Cheng J, Lu Y, et al. Hypersensitive MR angiography based on interlocking stratagem for diagnosis of cardiac-cerebral vascular diseases. Nat Commun. 2023;14:6149.
46. Li W, Cheng J, Zhang X, et al. High-resolution magnetic resonance angiography of tumor vasculatures with an interlocking contrast agent. ACS Nano. 2024;18:25647–56.
47. Xing H, Zhang S, Bu W, et al. Ultrasmall NaGdF4 nanodots for efficient MR angiography and atherosclerotic plaque imaging. Adv Mater. 2014;26:3867–72.
48. Wang J, Zhang H, Ni D, et al. High-performance upconversion nanoprobes for multimodal MR imaging of acute ischemic stroke. Small. 2016;12:3591–600.
49. He F, Zhu L, Zhou X, et al. Red blood cell membrane-coated ultrasmall NaGdF4 nanoprobes for high-resolution 3D magnetic resonance angiography. ACS Appl Mater Interfaces. 2022;14:26372–81.
50. Liu K, Yan X, Xu Y-J, et al. Sequential growth of CaF2:Yb, Er@CaF2: Gd nanoparticles for efficient magnetic resonance angiography and tumor diagnosis. Biomater Sci. 2017;5:2403–15.
51. Liu K, Cai Z, Chi X, et al. Photoinduced superhydrophilicity of Gd-doped TiO2 ellipsoidal nanoparticles boosts T1 contrast enhancement for magnetic resonance imaging. Nano Lett. 2022;22:3219–27.
52. Dong L, Xu Y-J, Sui C, et al. Highly hydrated paramagnetic amorphous calcium carbonate nanoclusters as an MRI contrast agent. Nat Commun. 2022;13:5088.
53. Liu C, Liu X, Wei Z, et al. Amorphous albumin gadolinium-based nanoparticles for ultrahigh-resolution magnetic resonance angiography. ACS Appl Mater Interfaces. 2024;16:9702–12.
54. Shin T-H, Kim PK, Kang S, et al. High-resolution T1 MRI via renally clearable dextran nanoparticles with an iron oxide shell. Nat Biomed Eng. 2021;5:252–63.
55. Shen Z, Wu A, Chen X. Iron oxide nanoparticle based contrast agents for magnetic resonance imaging. Mol Pharm. 2016;14:1352–64.
56. Israel LL, Galstyan A, Holler E, et al. Magnetic iron oxide nanoparticles for imaging, targeting and treatment of primary and metastatic tumors of the brain. J Control Release. 2020;320:45–62.
57. Wang YXJ. Current status of superparamagnetic iron oxide contrast agents for liver magnetic resonance imaging. World J Gastroenterol. 2015;21:13400.
58. Bao Y, Sherwood JA, Sun Z. Magnetic iron oxide nanoparticles asT-1contrast agents for magnetic resonance imaging. J Mater Chem C. 2018;6:1280–90.
59. Jeon M, Halbert MV, Stephen ZR, et al. Iron oxide nanoparticles as T1 contrast agents for magnetic resonance imaging: fundamentals, challenges, applications, and prospectives. Adv Mater. 2020;33:1906539.
60. Kim BH, Lee N, Kim H, et al. Large-scale synthesis of uniform and extremely small-sized iron oxide nanoparticles for high-resolution T1 magnetic resonance imaging contrast agents. J Am Chem Soc. 2011;133:12624–31.
61. Lu Y, Xu YJ, Zhang GB, et al. Iron oxide nanoclusters for T1 magnetic resonance imaging of non-human primates. Nat Biomed Eng. 2017;1:637–43.

62. Toth GB, Varallyay CG, Horvath A, et al. Current and potential imaging applications of ferumoxytol for magnetic resonance imaging. Kidney Int. 2017;92:47–66.
63. Finn JP, Nguyen KL, Hu P. Ferumoxytol vs. gadolinium agents for contrast-enhanced MRI: thoughts on evolving indications, risks, and benefits. J Magn Reson Imaging. 2017;46:919–23.
64. Hope MD, Hope TA, Zhu C, et al. Vascular imaging with ferumoxytol as a contrast agent. Am J Roentgenol. 2015;205:W366–73.
65. Chin MS, Steigner M, Yin W, et al. Intraluminal assessment of coronary arteries with ferumoxytol-enhanced magnetic resonance angiography. JACC Cardiovasc Imaging. 2018;11:505–8.
66. Mukundan S, Steigner ML, Hsiao L-L, et al. Ferumoxytol-enhanced magnetic resonance imaging in late-stage CKD. Am J Kidney Dis. 2016;67:984–8.
67. Bashir MR, Bhatti L, Marin D, et al. Emerging applications for ferumoxytol as a contrast agent in MRI. J Magn Reson Imaging. 2014;41:884–98.
68. Finn JP, Nguyen KL, Han F, et al. Cardiovascular MRI with ferumoxytol. Clin Radiol. 2016;71:796–806.
69. Stabi KL, Bendz LM. Ferumoxytol use as an intravenous contrast agent for magnetic resonance angiography. Ann Pharmacother. 2011;45:1571–5.
70. Nguyen K-L, Yoshida T, Kathuria-Prakash N, et al. Multicenter safety and practice for off-label diagnostic use of ferumoxytol in MRI. Radiology. 2019;293:554–64.
71. Ahmad F, Treanor L, McGrath TA, et al. Safety of Off-label use of ferumoxtyol as a contrast agent for MRI: a systematic review and meta-analysis of adverse events. J Magn Reson Imaging. 2020;53:840–58.
72. Aguilera AI, Wetmore JB, Weinhandl ED, et al. Relative incidence of acute adverse events with ferumoxytol compared to other intravenous iron compounds: a matched cohort study. PLoS ONE. 2017;12:e0171098.
73. Sun W, Liu W, Zhang Z, et al. Asymmetrical cortical vessel sign on susceptibility-weighted imaging: a novel imaging marker for early neurological deterioration and unfavorable prognosis. Eur J Neurol. 2014;21:1411–8.
74. Jiang H, Zhang Y, Pang J, et al. Susceptibility-diffusion mismatch correlated with leptomeningeal collateralization in large vessel occlusion stroke. J Int Med Res. 2021;49:3000605211013179.
75. Lee HJ, Roh HG, Lee SB, et al. Collateral estimation by susceptibility-weighted imaging and prediction of functional outcomes after acute anterior circulation ischemic stroke. Sci Rep. 2021;11:21370.
76. Chavhan GB, Babyn PS, Thomas B, et al. Principles, techniques, and applications of T2*-based MR imaging and its special applications. Radiographics. 2009;29:1433–49.
77. Liu S, Buch S, Chen Y, et al. Susceptibility-weighted imaging: current status and future directions. NMR Biomed. 2017;30:e3552.
78. Vigneau-Roy N, Bernier M, Descoteaux M, et al. Regional variations in vascular density correlate with resting-state and task-evoked blood oxygen level-dependent signal amplitude. Hum Brain Mapp. 2013;35:1906–20.
79. Yang A, Zhuang H, Du L, et al. Evaluation of whole-brain oxygen metabolism in Alzheimer's disease using QSM and quantitative BOLD. Neuroimage. 2023;282: 120381.
80. Yablonskiy DA, Sukstanskii AL, He X. Blood oxygenation level-dependent (BOLD)-based techniques for the quantification of brain hemodynamic and metabolic properties—theoretical models and experimental approaches. NMR Biomed. 2012;26:963–86.
81. Buch S, Wang Y, Park M-G, et al. Subvoxel vascular imaging of the midbrain using USPIO-Enhanced MRI. Neuroimage. 2020;220: 117106.
82. Jung H, Park B, Lee C, et al. Dual MRI T1 and T2(∗) contrast with size-controlled iron oxide nanoparticles. Nanomed-Nanotechnol. 2014;10:1679–89.
83. Kim SG, Harel N, Jin T, et al. Cerebral blood volume MRI with intravascular superparamagnetic iron oxide nanoparticles. NMR Biomed. 2012;26:949–62.
84. Wang T, Hou Y, Bu B, et al. Timely visualization of the collaterals formed during acute ischemic stroke with Fe3O4 nanoparticle-based MR imaging probe. Small. 2018;14:1800573.
85. Engelter ST, Provenzale JM, Petrella JR, et al. Use of exponential diffusion imaging to determine the age of ischemic infarcts. J Neuroimaging. 2001;11:141–7.
86. Wang XY, Noguchi K, Takashima S, et al. Serial diffusion-weighted imaging in a patient with MELAS and presumed cytotoxic oedema. Neuroradiology. 2003;45:640–3.
87. Copen WA, Morais LT, Wu O, et al. In acute stroke, can CT perfusion-derived cerebral blood volume maps substitute for diffusion-weighted imaging in identifying the ischemic core? PLoS ONE. 2015;10:e0133566.
88. Zhang P, Li W, Liu C, et al. Simultaneous identifying the infarct core, collaterals, and penumbra after acute ischemic stroke with a low-immunogenic MRI nanoprobe. Mater Design. 2023;233: 112211.
89. Han B, Zhao Y, Ma L, et al. A minimalist iron oxide nanoprobe for the high-resolution depiction of stroke by susceptibility-weighted imaging. Small. 2024;20:2401061.
90. Zhang P, Feng Y, Zhu L, et al. Predicting thrombolytic haemorrhage risk of acute ischemic stroke through angiogenesis/inflammation dual-targeted MR imaging. Nano Today. 2023;48: 101707.
91. Zhao Y, Pan J, Han B, et al. Ultrahigh-resolution visualization of vascular heterogeneity in brain tumors via magnetic nanoparticles-enhanced susceptibility-weighted imaging. ACS Nano. 2024;18:21112–24.
92. Zhang P, Guan J, Zhang N, et al. Visualizing the spatial distribution of inflammation in the depressed brain with a targeted MRI nanoprobe in vivo. NPG Asia Mater. 2023;15:58.
93. Wang H, Jiang Q, Shen Y, et al. The capability of detecting small vessels beyond the conventional MRI sensitivity using iron-based contrast agent enhanced susceptibility weighted imaging. NMR Biomed. 2020;33:e4256.
94. Neuwelt EA, Hamilton BE, Varallyay CG, et al. Ultrasmall superparamagnetic iron oxides (USPIOs): a future alternative magnetic resonance (MR) contrast agent for patients at risk for nephrogenic systemic fibrosis (NSF)? Kidney Int. 2009;75:465–74.
95. Shen Y, Hu J, Eteer K, et al. Detecting sub-voxel microvasculature with USPIO-enhanced susceptibility-weighted MRI at 7 T. Magn Reson Imaging. 2020;67:90–100.
96. Buch S, Subramanian K, Jella PK, et al. Revealing vascular abnormalities and measuring small vessel density in multiple sclerosis lesions using USPIO. NeuroImage-Clin. 2021;29:102525.
97. Dósa E, Tuladhar S, Muldoon LL, et al. MRI using ferumoxytol improves the visualization of central nervous system vascular malformations. Stroke. 2011;42:1581–8.
98. Liu S, Brisset JC, Hu J, et al. Susceptibility weighted imaging and quantitative susceptibility mapping of the cerebral vasculature using ferumoxytol. J Magn Reson Imaging. 2017;47:621–33.
99. Li W, Cheng J, Liu C, et al. Shine and darkle the blood vessels: multiparameter hypersensitive MR angiography for diagnosis of panvascular diseases. Sci Adv. 2024;10:eadq4082.
100. Zhang P, Jiao M, Li Y, et al. Bright semiconductor quantum dots shed new light on precision nanomedicine for various diseases. Small Sci. 2023;4:2300081.
101. Cai Y, Wei Z, Song C, et al. Optical nano-agents in the second near-infrared window for biomedical applications. Chem Soc Rev. 2019;48:22–37.
102. Huang X, Song J, Yung BC, et al. Ratiometric optical nanoprobes enable accurate molecular detection and imaging. Chem Soc Rev. 2018;47:2873–920.
103. Zhu S, Tian R, Antaris AL, et al. Near-infrared-II molecular dyes for cancer imaging and surgery. Adv Mater. 2019;31:1900321.
104. Hong G, Antaris AL, Dai H. Near-infrared fluorophores for biomedical imaging. Nat Biomed Eng. 2017;1:0010.
105. Fan Y, Zhang F. A new generation of NIR-II probes: lanthanide-based nanocrystals for bioimaging and biosensing. Adv Opt Mater. 2019;7:1801417.
106. Antaris AL, Chen H, Diao S, et al. A high quantum yield molecule-protein complex fluorophore for near-infrared II imaging. Nat Commun. 2017;8:15269.
107. Sun J, Cai W, Sun Y, et al. Facile synthesis of melanin-dye nanoagent for NIR-II fluorescence/photoacoustic imaging-guided photothermal therapy. Int J Nanomed. 2020;15:10199–213.
108. Cao J, Zhu B, Zheng K, et al. Recent progress in NIR-II contrast agent for biological imaging. Front Bioeng Biotech. 2020;7:487.

109. Liu S, Li Y, Kwok RTK, et al. Structural and process controls of AIEgens for NIR-II theranostics. Chem Sci. 2021;12:3427–36.
110. Hong G, Lee JC, Robinson JT, et al. Multifunctional in vivo vascular imaging using near-infrared II fluorescence. Nat Med. 2012;18:1841–6.
111. Ma Z, Zhang M, Yue J, et al. Near-infrared IIb fluorescence imaging of vascular regeneration with dynamic tissue perfusion measurement and high spatial resolution. Adv Funct Mater. 2018;28:1803417.
112. Guo Y, Hu J, Wang P, et al. In vivo NIR-II fluorescence lifetime imaging of whole-body vascular using high quantum yield lanthanide-doped nanoparticles. Small. 2023;19:2300392.
113. Zhong Y, Ma Z, Zhu S, et al. Boosting the down-shifting luminescence of rare-earth nanocrystals for biological imaging beyond 1500 nm. Nat Commun. 2017;8:737.
114. Xue Z, Zeng S, Hao J. Non-invasive through-skull brain vascular imaging and small tumor diagnosis based on NIR-II emissive lanthanide nanoprobes beyond 1500 nm. Biomaterials. 2018;171:153–63.
115. Chen D, Qi W, Liu Y, et al. Near-infrared II semiconducting polymer dots: chain packing modulation and high-contrast vascular imaging in deep tissues. ACS Nano. 2023;17:17082–94.
116. Ren F, Ding L, Liu H, et al. Ultra-small nanocluster mediated synthesis of Nd 3+ -doped core-shell nanocrystals with emission in the second near-infrared window for multimodal imaging of tumor vasculature. Biomaterials. 2018;175:30–43.
117. Li Y, Zhang P, Ning H, et al. Emitting/sensitizing ions spatially separated lanthanide nanocrystals for visualizing tumors simultaneously through up- and down-conversion near-infrared II luminescence in vivo. Small. 2019;15:1905344.
118. Fang Z, Wang C, Yang J, et al. Oxyhaemoglobin saturation NIR-IIb imaging for assessing cancer metabolism and predicting the response to immunotherapy. Nat Nanotechnol. 2023;19:124–30.
119. Yang Y, Chen M, Wang P, et al. Highly thermal stable RNase A@PbS/ZnS quantum dots as NIR-IIb image contrast for visualizing temporal changes of microvasculature remodeling in flap. J Nanobiotechnol. 2022;20:128.
120. Zhang R, Shen P, Xiong Y, et al. Bright, photostable and long-circulating NIR-II nanoparticles for whole-process monitoring and evaluation of renal transplantation. Natl Sci Rev. 2024;11:nwad286.
121. Sheng Z, Li Y, Hu D, et al. Centimeter-deep NIR-II fluorescence imaging with nontoxic AIE probes in nonhuman primates. Research. 2020;2020:4074593.
122. Hu Z, Fang C, Li B, et al. First-in-human liver-tumour surgery guided by multispectral fluorescence imaging in the visible and near-infrared-I/II windows. Nat Biomed Eng. 2019;4:259–71.
123. Zhang Z, Fang C, Zhang Y, et al. NIR-II nano fluorescence image guided hepatic carcinoma resection on cirrhotic patient. Photodiagn Photodyn Ther. 2022;40:103098.
124. Cao C, Jin Z, Shi X, et al. First clinical investigation of near-infrared window IIa/IIb fluorescence imaging for precise surgical resection of gliomas. IEEE Trans Biomed Eng. 2022;69:2404–13.
125. Cao C, Deng S, Wang B, et al. Intraoperative near-infrared II window fluorescence imaging-assisted nephron-sparing surgery for complete resection of cystic renal masses. Clin Transl Med. 2021;11: e604.
126. Wu Y, Suo Y, Wang Z, et al. First clinical applications for the NIR-II imaging with ICG in microsurgery. Front Bioeng Biotech. 2022;10:1042546.
127. Song X, Gong H, Yin S, et al. Ultra-small iron oxide doped polypyrrole nanoparticles for in vivo multimodal imaging guided photothermal therapy. Adv Funct Mater. 2013;24:1194–201.
128. Jing L, Ding K, Kershaw SV, et al. Magnetically engineered semiconductor quantum dots as multimodal imaging probes. Adv Mater. 2014;26:6367–86.
129. Rosenkrans ZT, Ferreira CA, Ni D, et al. Internally responsive nanomaterials for activatable multimodal imaging of cancer. Adv Healthc Mater. 2020;10:2000690.
130. Sindhwani S, Chan WCW. Nanotechnology for modern medicine: next step towards clinical translation. J Intern Med. 2021;290:486–98.
131. Feliu N, Docter D, Heine M, et al. In vivo degeneration and the fate of inorganic nanoparticles. Chem Soc Rev. 2016;45:2440–57.
132. Soo Choi H, Liu W, Misra P, et al. Renal clearance of quantum dots. Nat Biotechnol. 2007;25:1165–70.
133. Liu C, Gao Z, Zeng J, et al. Magnetic/upconversion fluorescent NaGdF4:Yb, Er nanoparticle-based dual-modal molecular probes for imaging tiny tumors in vivo. ACS Nano. 2013;7:7227–40.
134. Poon W, Zhang Y-N, Ouyang B, et al. Elimination pathways of nanoparticles. ACS Nano. 2019;13:5785–98.

Publisher's Note